Sentinel-2 and MODIS land surface temperature-based evapotranspiration for irrigation efficiency calculations

DANIEL KILUU KYALO
FEBRUARY, 2017

SUPERVISORS:
Dr. Zoltan Vekerdy
Dr. Ir. Rogier Van der Velde

SENTINEL-2 AND MODIS LAND SURFACE TEMPERATURE BASED EVAPOTRANSPIRATION FOR IRRIGATION EFFICIENCY CALCULATIONS

DANIEL KILUU KYALO
Enschede, The Netherlands, February, 2017

Thesis submitted to the Faculty of Geo-Information Science and Earth Observation of the University of Twente in partial fulfilment of the requirements for the degree of Master of Science in Geo-information Science and Earth Observation.
Specialization: Water Resources and Environmental Management

SUPERVISORS:
Dr. Zoltan Vekerdy
Dr. Ir. Rogier van der Velde

THESIS ASSESSMENT BOARD:
Dr. Ir. Christiaan van der Tol (Chair)
Dr. Vu Hien Phan (External Examiner, Ho Chi Minh City University)

ABSTRACT

Water resource are not equitably distributed in space and time. This creates competition for the resources especially in arid and semi-arid areas, and consequently the risk of overexploiting them. This risk becomes more complex when there are irrigation systems in these areas. This is because any imbalance in the regional water balance in the region is attributed to the abstractions of the irrigation systems. As a result, there is need for effective and efficient management water resources in such areas, which requires good knowledge of the hydrological fluxes. The field of remote sensing has been advancing, with new satellites, such as Sentinel-2, being introduced progressively; and consequently, providing new possibilities of getting a better understanding of the hydrological processes at a higher spatial-temporal resolution.

The Surface Energy Balance System (SEBS) was used to derive high resolution (10 m) evapotranspiration maps for the lower Catchment of Naivasha; which were consequently used to estimate the irrigation efficiency of open irrigation systems in the area. The high-resolution images were derived using Sentinel-2 data, downscaled MODIS land surface temperature and meteorological inputs obtained from KWSTI flux tower.

Two farms were considered in the analysis of irrigation efficiency, namely: Gorge farm and FHK Kingfisher farm. The analysis found that generally the farms were less efficient when the aridity index was high, that is during the rainy season, and especially in January and September. Gorge farm was found to have an irrigation efficiency of approximately 77 %, as compared to FHK Kingfisher farm which had an irrigation efficiency of 45%. Given that the farms have different irrigation systems, it implies that Gorge farm has more efficient irrigation systems/practices.

Keywords: Sentinel-2, actual evapotranspiration, MODIS land surface temperature, downscaling, irrigation efficiency.

DEDICATION

To my Dad Jeremiah K. Kitaa, and mom Veronicah Kyalo, you have been a great source of encouragement.

.

ACKNOWLEDGEMENTS

I gladly take this opportunity to thank God for this far He has brought me, and for giving me the strength to face each day with a smile.

Secondly, I am most grateful to the Dutch government for financing my Msc. Studies through the NFP scholarship programme. It has been a nice experience.

This process would not have been possible without the dedication of the ITC staff, and at this point I have to single out the input of my supervisors; Dr. Zoltan Vekerdy and Dr. Ir. Rogier van der Velde for shaping me through this research. Special thanks to Dr. Zoltan for keeping your door and skype open for consultation. You have been a great source of direction in this process, and I always came out of your office with a solution. To Dr. Rogier van der Velde, your advice and insight was always eye opening, I am most grateful for your assistance.

I sincerely appreciate the input of the wonderful people I had an opportunity to work with during my field work. Dr. Joost to begin with, thank you for helping with the installation of the Bowen ratio stations, sharing your knowledge, and for being an important link to the farms. In addition, I do recognize and appreciate the input of Dominic Wambua and Henry Munyaka, you went out of your way to help with the fieldwork, and treated the whole process as if it was your own. I also have to recognize the input of Dr. Vincent Odongo, for providing the flux tower data, as well as WRMA for the precipitation data.

Special recognition to the farms, that is, Gorge farm and its staff, in particular Gareth for allowing the installation of equipment in the farm and Paul Wamalwa for helping me out with the data. I also acknowledge Kingfisher farm for providing me with irrigation data.

To my WREM friends, J.Mutinda, Calisto, Kennedy, P. Wakhungu, P.Petulo thank you being great brothers and for the fun.

I also acknowledge the Kenyan community and friends among them Loise, Fred, Nick, Muiruri thanks for the fun moments.

I reserve special thanks to Njuki Sammy, both as a friend and for being available for consulation.

Sincere appreciation to the one precious friend Norah, thank you for your patience and understanding. To the Kyalo family, I am grateful for the love and support.

TABLE OF CONTENTS

1. Introduction 1
   1.1. Background 1
   1.2. Problem Statement 2
   1.3. Objectives 2
   1.4. Research questions 2
   1.5. Justification 3

2. Literature review 5
   2.1. Surface energy balance models 5
   2.2. Surface energy balance system 5
   2.3. Downscaling land surface temperature 6
   2.4. Irrigation efficiency 7
   2.5. Evapotranspiration 8

3. Study area 9
   3.1. Location 9
   3.3. Hydrology 10
   3.4. Irrigation 10

4. Research methods 11
   4.1. Field work and data collection 12
   4.2. Precipitation data 12
   4.3. Satellite data and preprocessing 13
   4.4. Retrieval of actual evapotranspiration in SEBS 16
   4.5. Validation of SEBS evapotranspiration 22
   4.6. CHIRPS Bias analysis and correction 25
   4.7. Computation of irrigation efficiency 26

5. Results and discussion 29
   5.1. Downscaled land surface temperature 29
   5.2. Evapotranspiration 30
   5.3. SEBS monthly evapotranspiration 36
   5.4. Computation of irrigation efficiency 38

6. Conclusion and recommendations 43
   6.1. Conclusion 43
   6.2. Recommendations 43

LIST OF FIGURES

Figure 1: Study Area highlighting the location of the farms and some of the rainfall gauging stations within the Study area (Njuki, 2016)......9
Figure 2: Research method flow chart 11
Figure 3: Installation of Bowen ratio and soil moisture sensors in Gorge farm 12
Figure 4: Monthly precipitation totals for five stations considered for bias correction...... 13
Figure 5 Sen2Cor atmospheric correction processing flow (Mueller Wilm, 2016)...... 14
Figure 6: Land cover classification map for the lower basin...... 18
Figure 7: SEBS model set-up for retrieval of March 11^{th} ET...... 20
Figure 8: Correlation between flux tower net radiation and daily evapotranspiration. 21
Figure 9: Energy balance closure analysis...... 23
Figure 10: Comparison between the uncorrected H-based ET (ET_Uncor), the corrected H-based ET (ET_cor) and the net radiation-based ET 24
Figure 11: Downscaled and original land surface temperature. The downscaled map shows more spatial variability of LST, without deviating from the maximum and minimum temperature-range of the original the image by a large margin...... 29
Figure 12: Sensitivity analysis of SEBS inputs 31
Figure 13: Comparison between air temperature at Gorge farm and KWSTI 32
Figure 14: Flux tower foot print showing the 80% source area...... 33
Figure 15: Validation of SEBS ET over non-irrigated areas 33
Figure 16: Validation of SEBS-ET in the irrigated area using Hargreaves ETp obtained by multiplying Hargreaves $ET0$ by Kc...... 35
Figure 17: Validation of SEBS using evaporative fraction...... 36
Figure 18: Monthly evapotranspiration maps. 37
Figure 19: Analysis of CHIRPS daily timescale bias...... 38
Figure 20: Monthly analysis of CHIRPS rainfall product bias 39

LIST OF TABLES

Table 1: Summary of some of the data obtained from the farms 12
Table 2: Summary of satellite data 13
Table 3 Aggregated NDVI classes 17
Table 4: Roughness of momentum transfer parameterization 18
Table 5: Error analysis comparing Rn_based ETa to ET_cor (corrected sensible heat-based ETa) 24
Table 6: Variation of air temperature between Gorge farm and KWSTI 32
Table 7: Validation of SEBS ET over Savannah vegetation 34
Table 8: Statistical analysis on the performance of SEBS in the irrigated areas 35
Table 9: Validation of SEBS evaporative fraction using Bowen ratio stations 36
Table 10 Performance of CHIRPS product at a daily timescale 39
Table 11 Performance of CHIRPS at a monthly time scale 40
Table 12 Summary of irrigation water consumption 40
Table 13: Breakdown of irrigation efficiency 40

LIST OF ABBREVIATIONS

LST	Land Surface Temperature
ET	Evapotranspiration
CHIRPS	Climate Hazards Group Infrared Precipitation with Station data
DSSF	Downward Shortwave Surface Flux
GDAL	Geospatial Data Abstraction Library
TIFF	Tagged Image File Format
GPS	Global Positioning System
HDF	Hierarchical Data Format
ECMWF	European Centre for Medium-Range Weather Forecasts
ILWIS	Integrated Land and Water Information System
NetCDF	Network Common Data Form
NIR	Near Infrared
PBL	Planetary Boundary Layer
SEBS	Surface Energy Balance System
MODIS	Moderate Resolution Imaging Spectro-radiometer
SRTM	Shuttle Radar Topography Mission
WRMA	Water Resources Management Authority
KWSTI	Kenya Wildlife Training Institute
USGS	United States Geological Survey
HB	Hit Bias
MB	Miss Bias
FB	False Bias
BF	Bias Factor
LSA SAF	Land Surface Analysis Satellite Applications Facility
OLI	Operational Land Imager
NDVI	Normalized Difference Vegetation Index
TIR	Thermal Infrared
TOA	Top of Atmosphere
S-SEBI	Simplified Surface Energy Balance Index
SSR	Surface net Solar Radiation
STR	Surface net Thermal Radiation
CCD	Cold Cloud Duration
FVC	Fractional Vegetation Cover
EUMETSAT	European Centre for Medium-Range Weather Forecasts

1. INTRODUCTION

1.1. Background

According to FAO (2003) a large percentage of the economically accessible water is already committed. Out of the committed economically accessible water, human abstraction accounts for over 60%, with the other percentage being what must remain in the reservoirs. Considering that water is not equally distributed in time and space, it implies that almost all the economically accessible water is already committed.

Agriculture is the main consumer of water in the world, and accounts for close to 70% of global abstractions (FAO, 2003). The global efficiency of irrigation systems is estimated to be about 50% implying that most irrigation systems abstract close to double what they need (FAO, 2003). This means that it is possible to increase the proportion of economically accessible water by improving the efficiency of irrigation systems.

.

Surface water resources in arid and semi-arid regions are mostly at risk of overexploitation because irrigation in these areas; relies heavily on water drawn mainly from rivers and reservoirs (Wu, Zhou, Wang, Li, & Zhong, 2015). This, compounded by the big evapotranspiration deficit (resulting from the imbalance between precipitation and potential evapotranspiration) creates the necessity for effective and efficient management of the available water resources(Gokmen et al., 2013). To achieve this, the assessment of hydrological fluxes at basin/regional scale is mandatory to better capture the mechanisms affecting hydrological dynamics (Gokmen et al., 2013)

Jensen, (2007) states that to better manage irrigation water, it is important to clearly understand the governing water balance, which can be expressed by Equation (1.1)

$$W_g = E + T + R_s + \Delta S + D \tag{1.1}$$

where, W_g is the gross irrigation water supplied, E is the evaporation [mm], T is transpiration [mm], R_s is surface runoff [mm], ΔS is the change in soil moisture at the root-zone [mm] and D is percolation beyond the root-zone [mm]. These terms help in partitioning irrigation water into effective consumption and losses.

Akdim et al. (2014) points out that the general idea of using remote sensing to assess irrigation performance was conceived as early as the late 1980s. The complexity of collecting ground data continuously to assess the performance of irrigation systems and the cost implication was and still is the biggest drive to the use of remote sensing in estimating irrigation efficiency.

A study by Njuki (2016) successfully used Landsat 8 shortwave bands and MODIS Land Surface Temperature (LST) to assess irrigation performance of open irrigated farms in the lower Naivasha basin. In that study, he proposed an improvement in the validation of the derived SEBS evapotranspiration, to better quantify the uncertainties in estimating the actual evapotranspiration, especially over the irrigated areas. This thesis is thus a follow-up on the research by Njuki (2016).

1.2. Problem Statement

Lake Naivasha is a Ramsar site which supports a diverse ecosystem, besides being an important economic resource. According to Odongo et al. (2014), the lake has experienced large variations in its water levels and at one time in the past came close to drying up. A study by Awange et al. (2013) shows that its water levels decreased by around 10.8% between 2006 and 2010, which corresponds to a 1.38m drop in water level. The lake supports various socioeconomic activities, with agriculture being the leading consumer of water from the lake.

The lake Naivasha basin has experienced a steady growth in population, drawn to the area by the flourishing horticulture industry. The growth in population has put more pressure on the water resource. According to Odongo et al. (2014), domestic and irrigation water demands account for over 70% of the water abstraction from the lake. Awange et al. (2013) state that the impact of the declining lake levels became more apparent in the 1990s when most of the farms were introduced in the basin

To properly manage the water resource, and clearly understand the cause(s) of lake level fluctuations in the lake, it is important to have accurate information of the hydrological fluxes in the area. This specifically includes knowledge on the precipitation, actual and potential evapotranspiration and how they are distributed in the area as proposed by Gokmen et al. (2013), for arid and semiarid areas. Given that most of the studies in the area have singled out irrigation as the main cause of lake level fluctuations, and considering the socio-economic importance of lake Naivasha; it is important to ascertain the efficiency of the irrigation systems in the basin, and possibly the effect of the farms on the hydrological dynamics of the lower basin.

This study builds on a previous research by Njuki, (2016), where he used Landsat 8 shortwave bands and MODIS LST to assess the performance of open irrigated farms in Naivasha. The study proposed that better validation measures should be used for the SEBS-derived evapotranspiration. This will be one of the improvements this study provides to the previous study, besides the fact that it will make use of Sentinel-2 data instead of Landsat 8. Moreover, given the mixed farming in the pivot irrigated farms, it was not easy to capture clearly the heterogeneity of evapotranspiration in the farms. As a result, this study will assess the applicability of using 10m resolution Sentinel-2 data to downscale 1km LST. In addition to this, Sentinel-2 data will be used together with the downscaled LST to derive actual evapotranspiration in SEBS and consequently estimate irrigation efficiency of open farms in Naivasha, at a higher spatial resolution.

1.3. Objectives

The main objective of the study is to estimate irrigation efficiency of open irrigated farms in Naivasha using Sentinel-2 and MODIS downscaled land surface temperature.

Specific objectives

- To downscale MODIS land surface temperature to the 10m resolution of Sentinel-2.
- To make reliable high-resolution estimates of evapotranspiration using Sentinel-2 data and MODIS LST.
- To estimate the efficiency of open irrigated farms in Naivasha.

1.4. Research questions

- How does the downscaled MODIS land surface temperature compare to the original LST map?
- How does evapotranspiration derived from remote sensing compare to that derived using in-situ measurements in the open irrigated farms?
- What is the efficiency of the irrigation systems?

1.5. Justification

Ma et al. (2012) state that combining remote sensing, in-situ data and land surface energy balance models such as the Surface Energy Balance System (SEBS), Surface Energy Balance Algorithm for Land (SEBAL) and the Simplified Surface Energy Balance Index (S-SEBI), is the most suitable way of estimating plant water use. To estimate irrigation water consumption, an accurate estimation of crop evapotranspiration is needed (Abdul Karim et al., 2013). Accurate estimates of irrigation water use are a necessity in planning how to manage water resources, and remote sensing offers an ideal/affordable avenue to achieve this (Singh et al., 2013). A study by Granell, Casteleyn, & Atzberger (2015) concludes that the major challenge of using remote sensing data is that most of it is too coarse to capture spatial variability at small scale level. It further recommends the use of high resolutions sensors like Sentinel-2, which also has a considerably high resolution.

There is need for consistent high resolution monitoring of hydrological fluxes in Naivasha as highlighted in Section 1.2. The possibility of using Sentinel-2 in combination with LST products from other satellites provides an additional alternative for monitoring hydrological fluxes. It also builds on a previous study by Njuki (2016), making Sentinel-2 an additional satellite to fill the gaps he encountered due to the considerably low revisit time of Landsat 8; which necessitated gap-filling using Hargreaves' reference evapotranspiration. During validation, SEBS-derived evapotranspiration was up-scaled to the flux tower footprint as recommended by Njuki (2016), making it more representative of the Savannah. Moreover, the images provided an increased spatial resolution in comparison to Landsat 8 data used by Njuki (2016), therefore the heterogeneity of the farms was captured better in this research. It was also important to ascertain the suitability of the high-resolution Sentinel-2 data for modelling hydrological processes in the area.

2. LITERATURE REVIEW

2.1. Surface energy balance models

The use of remote sensing to estimate evapotranspiration became operational in recent past, because it is less expensive than using ground measurements e.g. eddy covariance, and requires less ground data. There are a number of surface energy balance models, which include Surface Energy Balance Index (SEBI), Mapping Evapotranspiration at High Resolution and the with Internalized Calibration (METRIC), SEBS, SEBAL, T-SEBS, S-SEBI and T_s-VI among others (Liou & Kar, 2014; Lian & Huang, 2016). These models can be grouped into two main categories, that is: those that calculate latent heat flux as the remainder of the energy balance equation (calculate sensible heat flux first); and those that use an index to calculate relative evaporation (Z. Su, 2002). The models are based on the surface energy balance equation which can be expressed as shown in Equation (2.1) (Z. Su, 2002)

$$R_n = G + H + LE \tag{2.1}$$

Where R_n is the net radiation, *G* is the ground heat flux, and *LE* is the latent heat flux with the units for all these fluxes being $W\ m^{-2}$ (Liou & Kar, 2014). Energy balance models can be classified into two source and single source models, with one of their difference being that two-source models partition land surface temperature into soil and vegetation components (Liou & Kar, 2014).

A number of studies have been carried out to compare the performance of various single-source energy balance models, and have arrived at varied insightful conclusions. Lian & Huang, (2016) found SSEB and METRIC models performing reasonably well for oasis-desert regions. The major difference between the models is their accuracy when applied in different regions. Bhattarai, Shaw, Quackenbush, & Im, (2016) found SEBS to be the most appropriate model for use in humid subtropical climatic areas in a study where they tested five single source models. In the study, the accuracy of SEBS, SEBAL, METRIC and S-SEBI was found to be 75 to 82%. A study by Su et al., (2005) found out that the accuracy of the mean retrieved ET could be as high as 95% when higher resolution Landsat 7 ETM data was used in SEBS to estimate evapotranspiration. As a result, SEBS was considered the most ideal model for use in this research. Moreover, Njuki (2016) found that it performed reasonably well in a study carried out within the Kenyan Savannah.

2.2. Surface energy balance system

SEBS is a single-source energy balance model, which estimates the relative evaporation by means of an evaporative fraction, calculated with respect to the energy balance at limiting instances (Z. Su, 2002). The energy balance is expressed by Equation (2.1) where the net radiation, R_n , is computed using equation (2.2)

$$R_n = (1 - \alpha).R_{sw} + \varepsilon.R_{lw} - \varepsilon\sigma T_0^4 \tag{2.2}$$

where, α is the albedo [-], R_{sw} and R_{lw} is the incoming shortwave and longwave radiation respectively [W m^{-2}], ε is the emissivity [-] and T_0 is the land surface temperature [K].
The ground heat flux is expressed by equation (2.3)

$$G = R_n.\left(\Gamma_c + (1 - f_c).(\Gamma_s - \Gamma_c)\right) \tag{2.3}$$

where f_c is the fractional cover by canopy [-], $\Gamma_s = 0.05\ and\ \Gamma_c = 0.315$ and refer to the ratio of soil heat flux to net radiation for bare soil and under full vegetation cover respectively.

The evaporative fraction is derived by employing the concept that at the wet-limit, evaporation is at its maximum, with the available energy being the only limiting factor. On the other hand, at the dry-limit, soil moisture is very close to the wilting point, and thus evaporation becomes zero or negligible. This can be mathematically expressed by Equations (2.4) and (2.5)

$$\lambda E_{dry} = R_n - G_0 - H_{dry} \equiv 0 \tag{2.4}$$

$$H_{wet} = R_n - G_0 - \lambda E_{wet} \tag{2.5}$$

where H_{dry} is the sensible heat flux at the dry limit [W m-2], is H_{wet} is the sensible heat flux at the wet limit [W m-2] and λE_{wet} and λE_{dry} refers to the latent heat flux at the wet and dry limits respectively [W m-2]. From Equations (2.4) and (2.5), the relative evaporative fraction, Λ_r, is computed as shown by equation

$$\Lambda_r = \frac{\lambda E}{\lambda E_{wet}} = 1 - \frac{\lambda E_{wet} - \lambda E}{\lambda E_{wet}} \tag{2.6}$$

Equation (2.6) can be re-written as equation (2.7) by substituting equation(2.4) and (2.5)

$$\Lambda_r = 1 - \frac{H - H_{wet}}{H_{dry} - H_{wet}} \tag{2.7}$$

The sensible heat flux at the wet limit, H_{wet} is calculated using equation (2.8) as explained in (Z. Su, 2002).

$$\mathrm{H}_{wet} = \left((R_n - G_0) - \frac{\rho C_p}{r_{ew}} . \frac{e_s - e_a}{\gamma} \right) / \left(1 + \frac{\Delta}{\gamma} \right) \tag{2.8}$$

where ρ is the air density [Kg m-3], C_p is the specific heat capacity of air [J Kg-1 K-1], e_s and e_a are the saturation and actual vapor pressure respectively [Pa]; Δ is the rate of change of saturation vapor pressure with respect to temperature, γ is the psychrometric constant [Pa K-1] and r_{ew} is the external aerodynamic resistance at the wet limit case. The external resistance depends on the Obukhov length which is derived from a relation between the frictional velocity and sensible heat flux Z. Su (2002). The evaporative fraction is calculated using equation (2.9).

$$\Lambda = \frac{\lambda E}{R_n - G} = \frac{\Lambda_r . \lambda E_{wet}}{R_n - G} \tag{2.9}$$

Detailed explanations of the SEBS model is formulated are presented in Z. Su, (2002).

2.3. Downscaling land surface temperature

T Land Surface temperature is one of the parameters that highly influence the surface energy fluxes and consequently affect the accuracy of evapotranspiration estimation (Zhan et al., 2013; Liou & Kar, 2014). The advent of thermal remote sensing is largely considered a ground breaking innovation in the acquisition of LST at regional and global scale(Zhan et al., 2013; Zhang et al., 2016). The main challenge with thermal RS data is that most thermal sensor have a low spatial resolution, and thus poorly capture the heterogeneity of LST (Zhan et al., 2013). Landsat 8 OLI TIRS is one of the few high resolution thermal sensors with a spatial resolution of 100m resampled to 30 m (USGS, 2016). To derive evapotranspiration products at very high spatial resolution, the land surface temperature has to be downscaled, so as to reduce the thermal mixing effect caused by heterogeneity of the emitting surfaces.

There are various methods of downscaling which can be broadly classified into thermal sharpening and thermal un mixing (Zhan et al., 2013). The basic concept of disaggregation of LST is to retrieve the LST pattern by delineating the area of interest into a two-dimensional feature space; where one dimension represents LST and the other represents a reflectance parameter, e.g. vegetation index. Thermal sharpening is achieved by drawing statistical correlation between the low spatial resolution LST data with additional finer spatial resolution data e.g. NDVI of the same area, at a pixel by pixel level, to arrive at higher spatial resolution data. Thermal un-mixing on the other hand involves reconstructing the temperature of every component in the pixel using multi-spectral, temporal, angular or spatial observations.

2.4. Irrigation efficiency

T There are a number of terms used to define irrigation efficiency, all of which have slightly different meaning; they also include different parameters and assumptions in computation of irrigation efficiency. Jensen, (2007) identifies a number of terms which have been used to estimate irrigation efficiency. They include:

- Water application efficiency
- Net/effective irrigation efficiency
- Classical irrigation efficiency

2.4.1. Water application efficiency

This refers to the proportion of irrigation water which replenishes the soil moisture of the irrigated area as compared to the volume of irrigation water applied (Jensen, 2007). It is governed by the equation (2.10)

$$E_a = V_s/W_g \tag{2.10}$$

Where: E_a is the irrigation water application efficiency, V_s is the volume of irrigation water stored in the root zone and W_g is the volume of irrigation applied. The estimation of this efficiency is costly and time consuming as it requires field measurements of soil moisture, before and after irrigation (Jensen, 2007)

2.4.2. Net/effective irrigation efficiency

The net irrigation efficiency takes into account return flow from the irrigated area to the source of water e.g. river, lake or ground water. It is a measure of the beneficial use of irrigation water unconstrained by the irrigation purpose, and is governed by Equations (2.11) and (2.12)

$$E_e = E_n + f_r(1 - E_n) \tag{2.11}$$

$$E_n = V_c/W_g \tag{2.12}$$

where f_r is the fraction of return flow from the irrigated area, V_c is the volume of water beneficially used by the irrigation system, E_e is the net irrigation efficiency and E_n is irrigation efficiency with respect to V_c and W_g.

2.4.3. Classical irrigation efficiency

Classical irrigation efficiency is a measure of the proportion of water supplied to the irrigated area, which meets the crops evapotranspiration needs (Jensen, 2007). It is governed by Equation (2.13)

$$E_c = ET_a/(W_g - P_e) \tag{2.13}$$

where, E_c is the classical irrigation efficiency, ET_a is the actual evapotranspiration from the irrigated field and P_e is the effective rainfall.

2.5. Evapotranspiration

This is the process through which water moves from the surface of the earth to the atmosphere, and it is expressed as the sum of evaporation and transpiration(Jensen, 2007).

2.5.1. Reference evapotranspiration

It is the evapotranspiration (ET_0) from a grass reference surface that has certain characteristics, which include having a height of about 0.12m, is well watered and free from diseases (Allen, Pereira, Raes, & Smith, 1998). A number of methods can be used for estimating reference ET_0 which include, among others, Penman-Monteith, Hargreaves-Samani, Turc, Blaney Criddle, Makkink's and Modified Penman equations (Chauhan & Shrivastava, 2009; Allen et al., 1998; Feng et al., 2016; Ren, Qu, Martins, Paredes, & Pereira, 2016). The Penman-Monteith method is the most preferred method for estimating ET_0 (Abdul Karim et al., 2013); however, it requires a wide range of meteorological inputs making it unsuitable for areas with insufficient data (Ren et al., 2016). Different studies have made varied conclusions on the preferred alternative ET_0 method. Chauhan & Shrivastava (2009) identified Blaney-Criddle as the most appropriate alternative to Penman Monteith method, in a study carried out in Raipur; a tropical climate area. A study by Ren et al. (2016), on the other hand, shows large variations between Hargreaves-Samani equation and Penman-Monteith in arid areas, because the Hargreaves equation does not consider the effects of wind-speed.

2.5.2. Potential evapotranspiration

It refers to evapotranspiration, (ET_p), from a well-watered crop other than grass, which is limited only by the available energy, crop characteristics and the prevailing surface and atmospheric state (Z. Su, 2002; Perry, Steduto, Allen, & Burt, 2009). It is obtained by multiplying the reference evapotranspiration by a crop coefficient, K_c (Perry et al., 2009; Allen et al., 1998).

2.5.3. Actual evapotranspiration

This is the evapotranspiration (ET_a) that takes place under conditions of limited/fluctuating water availability in the soil; and is equivalent to the potential evapotranspiration adjusted for water stress using a stress factor K_s (Abdul Karim et al., 2013). The value of the stress factor ranges from 0 to 1.0 with 1 corresponding to ET_p, that is, when the crop is not under water stress, and 0, when the crop is fully stressed (Abdul Karim et al., 2013)

2.5.4. Effective rainfall

This refers to the contribution of rainfall to the crop water needs which reduces the amount of irrigation water that should be applied in an irrigated farm (Jensen, 2007)

3. STUDY AREA

3.1. Location

The study area is located in the Kenyan Rift Valley as shown in Figure 1, and the focus of this study is in the lower basin of the Lake Naivasha Catchment. This is because most of the farms are concentrated in the lower basin.

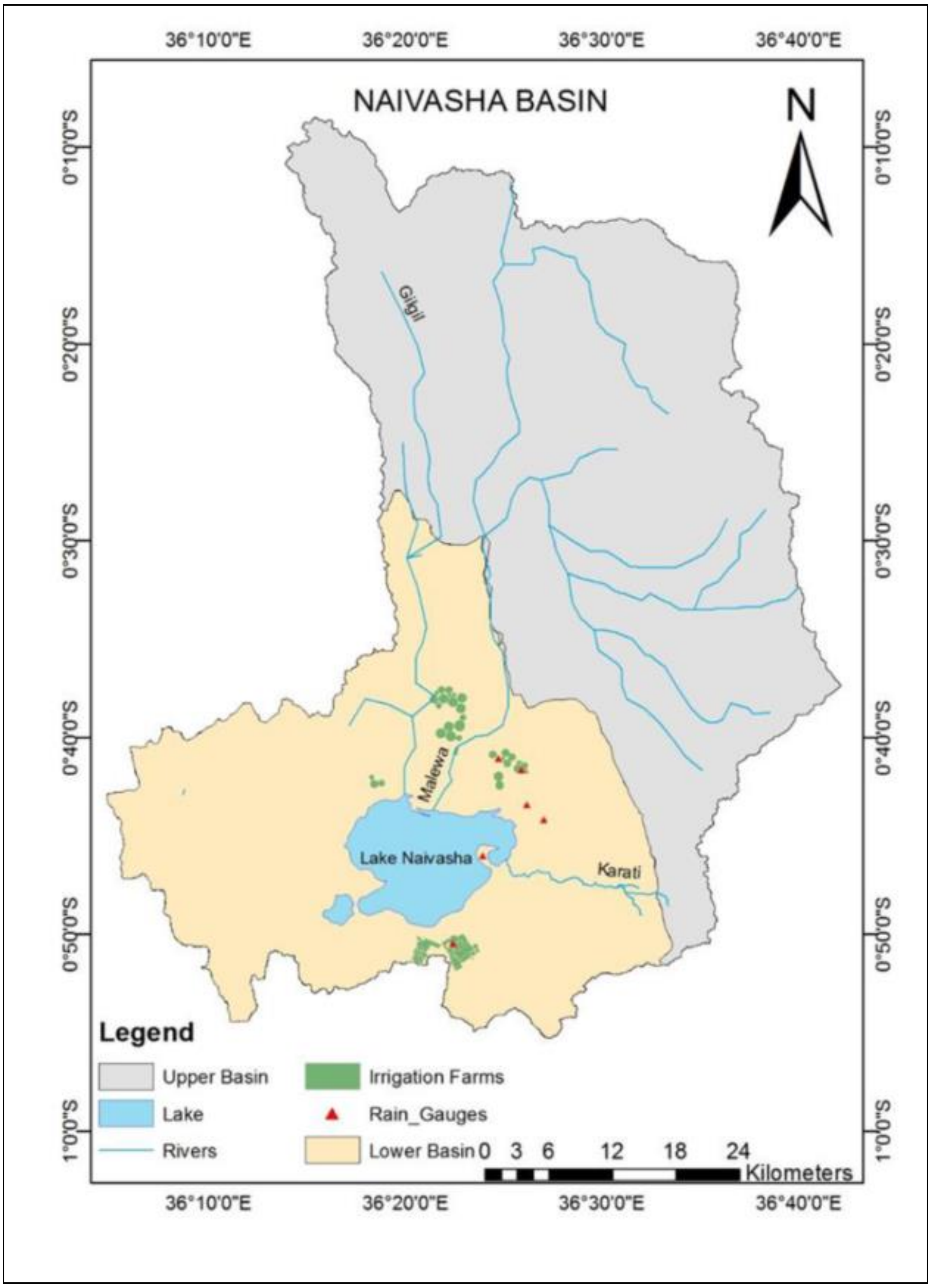

Figure 1: Study Area highlighting the location of the farms and some of the rainfall gauging stations within the Study area (Njuki, 2016)

3.2. Climate

The mean annual rainfall of the lower Naivasha Catchment is approximately 600 mm (Becht & Harper, 2002). It receives most of its precipitation within two major rain seasons, which are between the months: March to May and October to November (Odongo et al., 2014). Temperatures vary widely within the Basin with a daily minimum of 8 ˚C and maximum of 30 ˚C, on average.

3.3. Hydrology

Lake Naivasha is mainly recharged by two river systems, whose origin is at the north and north eastern high altitude parts of the catchment. It does not have an outlet at its surface and hence its major water outlets are by evaporation, underground flow and abstraction (Becht & Harper, 2002).

3.4. Irrigation

The total area under irrigation within the Lake Naivasha basin is around 4,450 ha, with over 80% of it being used for flower and vegetable farming (Mekonnen, Hoekstra, & Becht, 2012). Most of the farms are concentrated around the lower Naivasha Catchment, and draw their irrigation water either directly from the lake and the rivers that feed the lake, or from ground water. The impact of these abstractions has been largely viewed as a contributor to the lake level fluctuations.

4. RESEARCH METHODS

In this chapter, the methodologies applied to achieve the research objectives are discussed, and summarized in Figure 2.

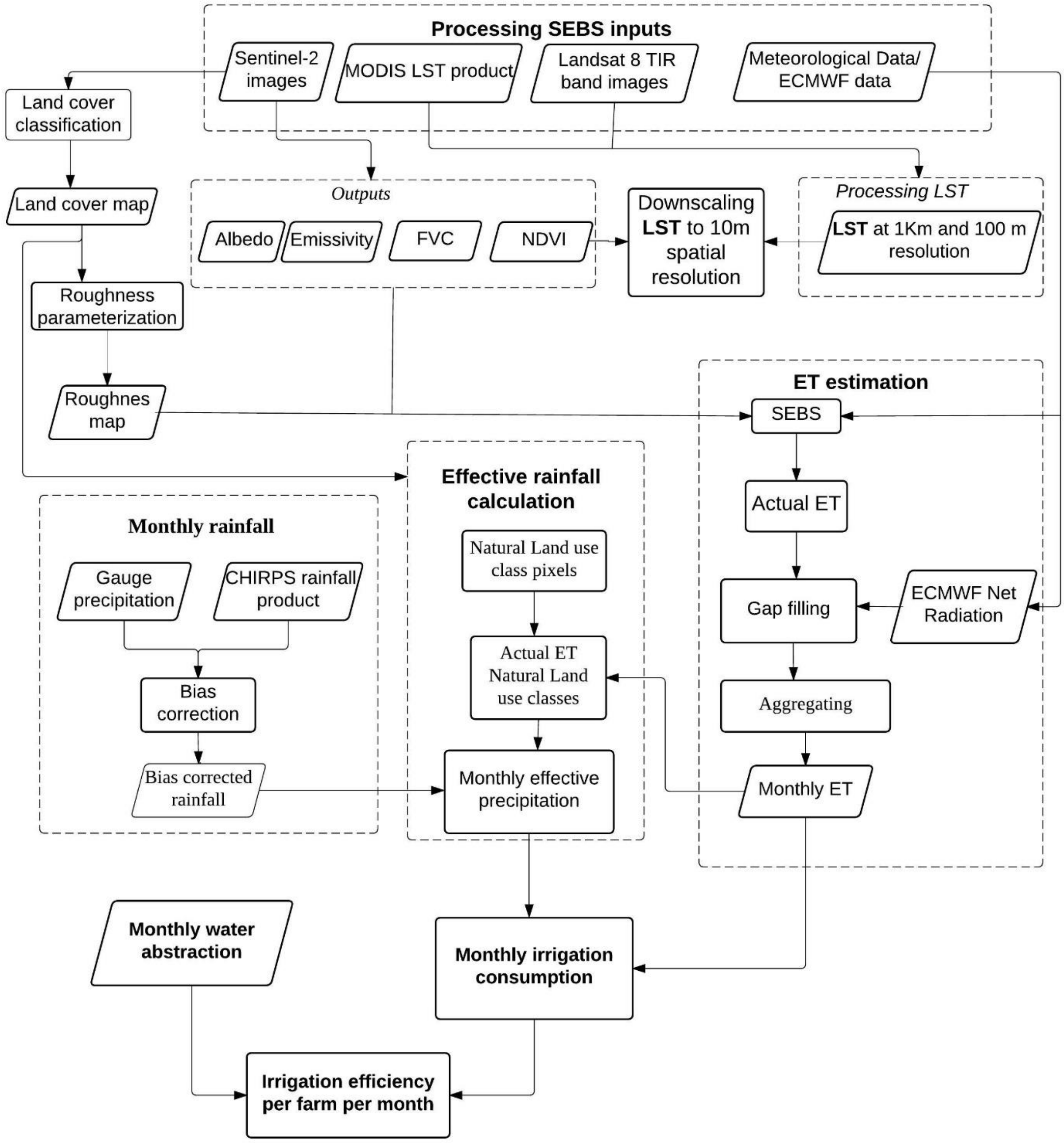

Figure 2: Research method flow chart

4.1. Field work and data collection

Field work was carried out between 13th September and 4th of October 2016, and was constrained to the farms within the lower catchment of Naivasha. During this time, two soil moisture sensors and two Bowen ratio stations were installed, as shown in Figure 3. Additional collected data included:

- Meteorological data from the flux tower for the year 2016.
- Crop types and farming practices including crop calendar and irrigation water consumption.
- Precipitation data from the Water Resources Management Authority (WRMA) and the farms.
- Land cover types around the farms.
- Water abstraction data from WRMA and water application data from the farms.
- GPS coordinates of the important locations on the farms and of rainfall gauging stations.

Table 1 shows some of the data obtained from the farms, crucial to this research.

Table 1: Summary of some of the data obtained from the farms

Farm	Area under pivot Irrigation (ha)	Area under other forms of irrigation e.g. drip irrigation	Crops grown	Source of water
Gorge Farm	240	226.8	Assorted vegetables	Lake and borehole
FHK Kingfisher veg Farm	_	130.25	Assorted vegetables	Lake

Figure 3: Installation of Bowen ratio and soil moisture sensors in Gorge farm

4.2. Precipitation data

Precipitation data was obtained both from WRMA and the farms around the lower basin. Out of these, only stations with the most consistent data were used for bias correction of CHIRPS rainfall data. From Figure 4, it is observed that consistent rainfall data from all the stations was available between January and June. This is because data for NYC gauging station had not been updated by WRMA since the end of June. Moreover, rainfall data could only be obtained for the period up to end of September 2016, given that the field work ended on 3rd October 2016. As a result, these are the months which were considered for obtaining a bias correction factor for correcting CHIRPS rainfall product, even though some stations had data up to end of September.

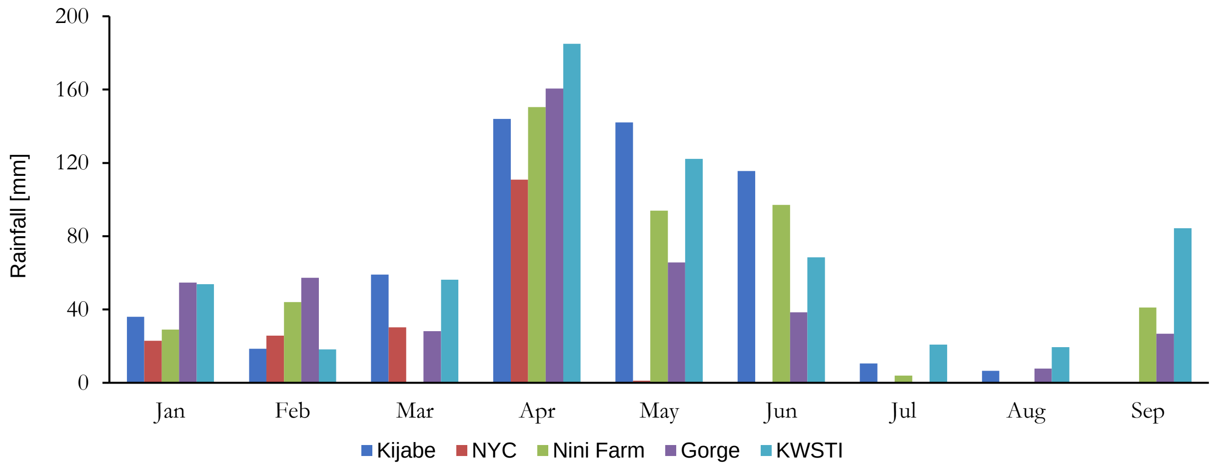

Figure 4: Monthly precipitation totals for five stations considered for bias correction

4.3. Satellite data and preprocessing

To derive actual evapotranspiration in SEBS, a number of satellite data inputs are required and they are summarized in Table 2.

Table 2: Summary of satellite data

Satellite Product	Source
Sentinel-2 and 3 data	https://scihub.copernicus.eu
Landsat 8 data	http://earthexplorer.usgs.gov/
Modis LST	https://lpdaac.usgs.gov/data_access/data_pool
SRTM DEM	http://earthexplorer.usgs.gov/
PBL height and net radiation	http://apps.ecmwf.int/datasets/data/interim-full-daily/levtype=sfc/
Sunshine hours	http://apps.ecmwf.int/datasets/data/interim-full-daily/levtype=sfc/
LSA shortwave flux (DSSF)	https://landsaf.ipma.pt/
CHIRPS rainfall product	http://chg.geog.ucsb.edu/data/index.html
Total column water vapor	http://apps.ecmwf.int/datasets/data/interim-full-daily/levtype=sfc/

4.3.1. Sentinel-2 data

Sentinel-2 images were used to derive a number of SEBS inputs including:

- Normalized Difference Vegetation Index (NDVI)
- Fraction of Vegetation Cover (FVC)
- Downscaling MODIS land surface temperature using NDVI
- Parameterizing emissivity using FVC
- Land cover classification map for parametrization of roughness height

Seven Sentinel-2 images with less than 20% cloud cover and corresponding to tile 36 and folder MZE of Sentinel-2 were downloaded for the year 2016. The images corresponded to the months January, February, March, August, September and October, meaning that there were no cloud free images from April to July. Consequently, these months were omitted in this research. The images were downloaded at Sentinel-2's 1C processing level, that is, Top of the Atmosphere (TOA) reflectance data (ESA, 2015). They were corrected for atmospheric effects using Sentinel's Sen2Cor method. Out of these images, those coinciding with August could not be used due to lack of flux tower meteorological data coinciding with the image acquisition dates.

4.3.2. Sentinel-2 atmospheric correction

Sentinel-2's Sen2Cor atmospheric correction tool was used to perform atmospheric correction of Sentinel-2 bands from TOA to surface reflectance. The tool relies on the flow process summarized in Figure 5. The atmospheric correction process involves four subtasks which include retrieval of aerosol optical thickness, water vapor, terrain and cirrus correction (Mueller Wilm, 2016).

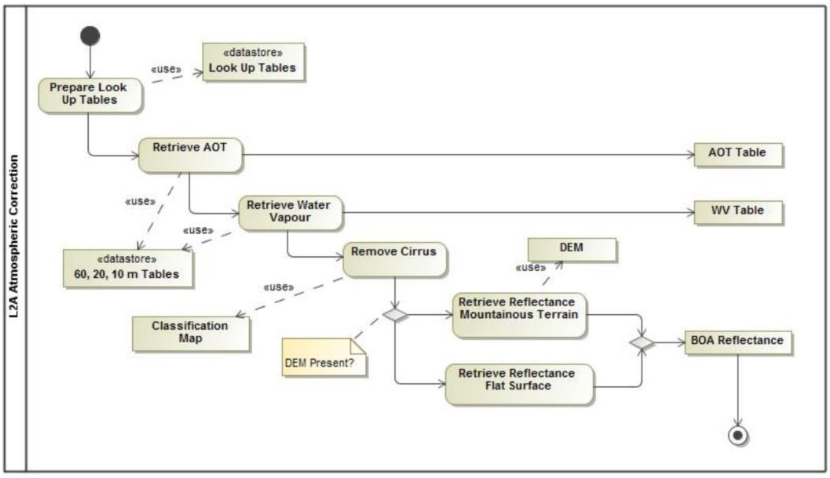

Figure 5 Sen2Cor atmospheric correction processing flow (Mueller Wilm, 2016)

Sen2Cor atmospheric correction model relies on computation of radiative transfer functions for various solar and sensor geometries, as well as terrain and atmospheric parameters. These parameters are generated through LibRadtran look up tables (Mueller Wilm, 2016). To perform the atmospheric correction, Sen2Cor was run in Python Anaconda and the atmospherically corrected images were converted from Jp2 format to GeoTIFF in the SNAP software, so that they could be imported into ILWIS. The imported Sentinel-2 images had reflectance values in integer format. To convert them to float reflectance values, a conversion factor provided in Sentinel-2 metadata was applied.

4.3.3. The Shuttle Radar Topography Mission data

The Shuttle Radar Topography Mission (SRTM) was launched in 2000 with the aim of acquiring high resolution digital elevation models for approximately 80 percent of the earth's surface (Farr et al., 2007). This mission is one of the few that provide free high resolution DEM data publicly at a spatial resolution as high as 30m (Hirt, Filmer, & Featherstone, 2010). A study by Hirt et al. (2010) found SRTM to be one of the best DEMs, with a root mean square error of about 6m. In addition, it found the SRTM data well suited for applications in a number of fields including hydrology. In this study, SRTM data was obtained as detailed in Table 2 and imported in ILWIS using GDAL. It was then resampled to 10 m spatial resolution of Sentinel-2.

4.3.4. ECMWF's ERA-Interim project data

Data on planetary layer height, sunshine hours and total column water vapor was obtained from ECMWF ERA-Interim as shown in Table 2. A more detailed description of ECMWF model and its performance is provided in Dee et al. (2011) and von Engeln, Teixeira, Engeln, & Teixeira (2013). The data was downloaded in NetCDF format at a resolution of 0.75^0 using SNAP software and converted to GeoTIFF format.

Net radiation data was required for derivation of monthly evapotranspiration maps, to be used in the gap-filling procedure explained in Section 4.4.9. It was obtained as the sum of ECMWF's daily Surface net Solar Radiation (SSR) and the daily Surface net Thermal Radiation (STR) for the same day, because ECMWF does not provide a net radiation as a product. These products were obtained at a resolution of 0.125˚. The daily net radiation was then divided by 86400 seconds to get the average net radiation [W m^{-2} s^{-1}].

4.3.5. MODIS land surface temperature product

The MODIS land surface temperature is derived using the split window algorithm, discussed in detail by Wan (1996). The split window algorithm is preferable because it reliably corrects for atmospheric effects, and has been found to have accuracies higher than 1 K in most cases (Wan, 1996). The MODIS products were downloaded from the site indicated in Table 2, for the tile specifications explained by Njuki (2016), because the study area and the data specifications are the same. The MODIS LST product, that is MOD11A1, was downloaded in HDF data format and an ILWIS script was used to convert it to GeoTIFF and ILWIS formats.

4.3.6. Landsat 8 Land surface temperature

Landsat 8 thermal bands were found to be affected by radiation outside the field of view, shortly after launch (USGS, 2016). Progress has been made to rectify this problem, with an update made in 2016, indicating that most of the Landsat 8 scenes contain valid thermal infrared data (USGS, 2016). Only one of Landsat 8's OLI TIR bands, band 10 has been of acceptable quality, with the other band not usable up to date. Retrieval of land surface temperature with Landsat 8 was done using the single channel algorithm proposed by Jiménez-Muñoz, Cristóbal, et al. (2009). This was the most preferable method because USGS still advices against the use of the split window algorithm, even after corrections for the stray light effect on the thermal bands (USGS, 2016).

4.3.7. Downward Surface Shortwave Flux

Down-welling shortwave flux (DSSF) refers to the radiation of wavelength range 0.3μm to 4.0 μm, reaching the surface of the Earth. It is largely influenced by the solar zenith angle and cloud cover. More detailed description of the EUMETSAT Satellite DSSF is given in LSA SAF, (2011) including the DSSF algorithm.

The DSSF product was downloaded from the site listed in Table 2, at full disk coverage, and at a spatial resolution of about 3km. The HDF-format DSSF product was then opened in Sentinel-2's SNAP software from where a submap of the study area was extracted and exported to GeoTIFF. The GeoTIFF DSSF products were then imported into ILWIS using GDAL, and resampled to Sentinel-2's 10m spatial resolution.

4.3.8. CHIRPS rainfall product

The Climate Hazards group Infrared Precipitation with Stations (CHIRPS) estimates rainfall based on observations of the infrared Cold Cloud Duration (CCD), and blends it with data from ground stations to improve the accuracy (Funk et al., 2015). According to a study conducted in Burkina Faso, West Africa, comparing different satellite based rainfall products; CHIRPS was found to be one of the best performing, with an $r^2 \geq 0.80$ at the decadal scale (Dembélé & Zwart, 2016).

The CHIRPS rainfall data was downloaded for the African region using the ISOD toolbox in ILWIS, for the year 2016. These maps were then sub mapped in ILWIS using the corner coordinates of the lower catchment shapefile. They were then grouped into monthly precipitation maps using the map list tool in ILWIS. The monthly map lists were aggregated to monthly precipitation maps using the ILWIS statistics operation.

4.4. Retrieval of actual evapotranspiration in SEBS

To retrieve actual evapotranspiration in SEBS the following inputs were first prepared.

4.4.1. Normalized Difference Vegetation Index

Normalized difference vegetation index was derived from Sentinel-2's bands 4 and 8, using equation (4.1)

$$NDVI = \frac{\rho_8 - \rho_4}{\rho_8 + \rho_4} \tag{4.1}$$

where ρ_8 and ρ_4 are the surface reflectance of Sentinel-2 bands in the near infrared and red spectrum ranges respectively [-].

4.4.2. Fraction of Vegetation Cover

Fraction of vegetation cover is one of the important parameters for estimating emissivity and describing surface processes. In this study, FVC was estimated using NDVI, derived in Equation (4.1), following Equation (4.2) proposed by Jiménez-Muñoz et al., (2009)

$$FVC = \frac{NDVI - NDVI_s}{NDVI_v - NDVI_s} \tag{4.2}$$

Where, $NDVI_s$ refers to bares soil NDVI and its values was set at 0.15 and $NDVI_v$ corresponds to the NDVI of closed vegetation canopy, and its value was chosen as the highest NDVI value in the map if it was greater than 0.91, else an $NDVI_v$ value of 0.91 was used; as recommended by Jiménez-Muñoz et al. (2009).

4.4.3. Emissivity map

Land surface emissivity was computed using Equation (4.3) proposed by Sobrino, Jiménez-Muñoz, & Paolini, (2004); where ε is the emissivity and FVC is the fractional vegetational cover.

$$\varepsilon = 0.004 * FVC + 0.986 \tag{4.3}$$

4.4.4. Albedo

Albedo is one of the parameters that affect the proportion of absorbed radiation, and consequently the apportioning of the incoming radiation into sensible, latent and ground heat flux (Liang, 2000). In this study, Sentinel-2 data was used to derive broad band albedo for the study area. However, since there was no land surface albedo algorithm for Sentinel-2 at the time of this analysis, an algorithm was derived using the Landsat 8 algorithm proposed by Liang et al. (2002). To derive it, Landsat 8 and Sentinel-2 images of coinciding acquisition date were used. The broadband albedo was first derived using the Landsat 8 algorithm and bands 2 to 7 of the OLI sensor. The Landsat 8 albedo subsets were divided with the corresponding Sentinel-2 reflectance subset-bands to obtain the Sentinel-2 algorithm. Equations (4.4) and (4.5)shows the Landsat 8 algorithm used and the derived Sentinel-2 albedo algorithm respectively.

$$\alpha_{OLI} = 0.356\rho_2 + 0.13\rho_4 + 0.373\rho_5 + 0.085\rho_6 + 0.072\rho_7 - 0.0018 \tag{4.4}$$

$$\alpha_{Sentinel-2} = 0.03\rho_2 + 0.11\rho_4 + 0.337\rho_8 + 0.065\rho_{11} + 0.054\rho_{12} - 0.0018 \quad (4.5)$$

4.4.5. Land surface temperature

Land Surface Temperature (LST) at 10m spatial resolution was obtained by downscaling MODIS LST product which is at a 1km spatial resolution. The disaggregation method involved deriving a linear correlation between MODIS LST and Sentinel-2's NDVI; following a disaggregation procedure proposed by Kustas, Norman, Anderson, & French, (2003). To achieve this, Sentinel-2's 10m resolution NDVI maps were first aggregated to the spatial resolution of MODIS LST. Using the fine resolution and the aggregated coarse resolution NDVI images, a coefficient of variation (standard deviation divided by the mean) was calculated for the aggregated NDVI pixels. This acted as an indicator of the level of homogeneity of the aggregated pixels. Using the coefficients, a subset of the aggregated pixels corresponding to a more homogeneous fine resolution surface was selected; that is, a surface whose aggregated NDVI pixels had the lowest coefficient of variation (Kustas et al., 2003). The selected subsets of aggregated NDVI pixels were then grouped into classes as shown in Table 3.

No.	NDVI Class	Description
1	$0.14 < NDVI_{aggregated} < 0.3$	Bare to sparse canopy cover
2	$0.31 < NDVI_{aggregated} < 0.4$	Partial canopy cover
3	$0.41 < NDVI_{aggregated} < 0.7$	Intermediate canopy cover
4	$NDVI_{aggregated} > 0.7$	Full canopy cover

Table 3 Aggregated NDVI classes

From the classes of aggregated NDVI classes in Table 3, a fraction of the pixels, approximately a quarter was picked from each class. The NDVI values of the selected pixels were used to fit a least squares expression between the aggregated Sentinel-2 NDVI and the coarse resolution MODIS LST as shown in equation (4.6), proposed by Kustas et al. (2003)

$$LST_{R1000}(NDVI_{1km}) = a + bNDVI_{R1000} \quad (4.6)$$

where $LST_{R1000}(NDVI_{1km})$ is the NDVI based LST at 1 km resolution, $NDVI_{R1000}$ is the aggregated I Km-resolution NDVI; a and b are the intercept and gradient of the linear regression.

To obtain the fine resolution LST, equation (4.6) was applied, replacing the coarse resolution NDVI with the fine resolution. The final fine resolution LST was obtained by applying a factor to account for deviations between $LST_{R1000}(NDVI_{1km})$ and the original MODIS LST product estimated using equation (4.7).

$$\Delta LST_{R1000} = LST_{MODIS} - LST_{R1000}(NDVI_{1km}) \quad (4.7)$$

The final fine resolution LST was obtained by applying a factor to account for deviations between $LST_{R1000}(NDVI_{1km})$ and the original MODIS LST product as shown by (4.8)

$$LST_{R10} = (a + bNDVI_{R10}) + \Delta LST_{R1000} \quad (4.8)$$

where: LST_{R10} is the final fine resolution LST [K], and $NDVI_{R10}$ is the 10 m resolution Sentinel-2 NDVI.

4.4.6. Roughness and momentum transfer parameters

The roughness, displacement and canopy heights were derived based on Sentinel-2 landcover classification maps for the lower Naivasha basin, done using Q-GIS. The maps were classified based on knowledge of the area gained during fieldwork and a previous landcover map by Vincent Odongo quoted in (Njuki, 2016). Values of roughness for momentum transfer, displacement and canopy height were obtained from a study by Wierenga, (1993). These values are summarized in Table 4. Due to the mixed farming practice in the open irrigated farms, average roughness values were chosen to represent vegetation in irrigated areas. Moreover, given that the aim of the study was to estimate irrigation efficiency in open irrigated farms; classification was done with a bias of accurately representing the irrigated areas.

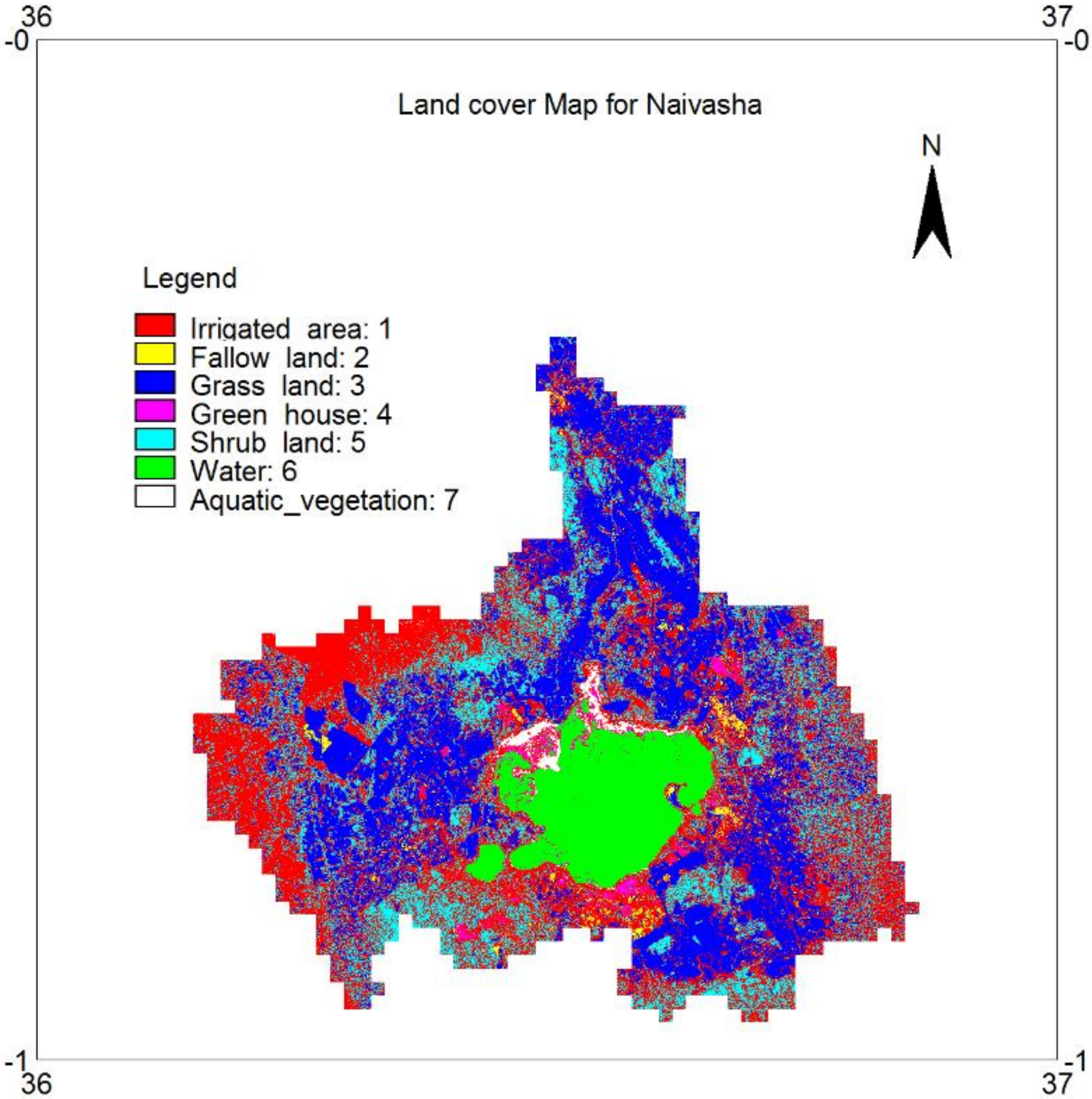

Figure 6: Land cover classification map for the lower basin

Maps of roughness length, canopy height and displacement height were obtained by assigning the land cover map, Figure 6, roughness values obtained from Table 4.

Table 4: Roughness of momentum transfer parameterization

Surface	Roughness length for	Canopy height [m]	Displacement height

	momentum transfer (Z0m) [m]		**(d0) [m]**
Very flat surface	0.00035	0.000	0.000
Fallow ground	0.0025	0.000	0.000
Short grass, moss, Bare farmland	0.019	0.03	0.021
Long grass, heather	0.04	0.44	0.308
Low mature crop	0.095	0.25	0.175
High mature crops	0.095	0.25	0.175
Continuous bushland	0.4	2.3	1.61
Dense low building	0.55	3.5	2.45
Water	0.00035	0.00	0.00
Green houses/horticultural areas	0.55	3.2	2.24
Aquatic	0.60	0.391	0.2737
Grassland	0.03	0.02	0.013
Farm land	0.25	0.04	0.163
Shrubs	0.35	1.8	1.173

4.4.7. Meteorological input

Meteorological data was obtained from a flux tower located at Kenya Wildlife Training Institute (KWSTI) grounds as well as Bowen ratio stations and soil moisture sensors installed in Gorge farm on 26th of September 2016, during field work. The KWSTI tower data was used with the assumption that it was representative of the farms, due to its close proximity to the farms; that is about 15 kilometers. The data obtained included atmospheric pressure, air temperature, wind speed, and relative humidity data. This data was used to compute specific humidity using Equation (4.9) proposed by Brutsaert, (2005).

$$q = \frac{\rho_v}{\rho} \tag{4.9}$$

where q is the specific humidity [-], ρ_v is the vapor density [kg m^{-3}] and ρ is the total air density [kg m^{-3}]. Equation (4.10) and (4.11) were used to compute the density of water vapor and air respectively

$$\rho_v = \frac{0.622e}{R_d T} \tag{4.10}$$

$$\rho = \frac{P}{R_d T}\left(1 - \frac{0.378e_a}{P}\right) \tag{4.11}$$

where e_a is measured in hPa, R_d is the specific gas constant [J Kg^{-1} K^{-1}]; P and T are the air pressure and Temperature in Pascals and K respectively. To calculate the water vapor pressure, saturated vapor pressure was first calculated using equation (4.12)

$$e_s = 6.108.exp\left(\frac{17.27T_a}{23T_a 7.3 +}\right) \tag{4.12}$$

where, T_a is the air temperature in ˚C and e_s is measured in hPa.

The water vapor pressure was then calculated using equation (4.13)

$$e = e_s * RH \tag{4.13}$$

where: RH is the relative humidity, which was obtained from the flux tower and Bowen ratio stations. Other satellite based meteorological inputs were derived as discussed in section 4.3.

4.4.8. Retrieval of daily evapotranspiration in SEBS

Daily evapotranspiration maps were obtained for the days which coincided with cloud-free MODIS satellite derived land surface temperature; and were within 5 days before or after the acquisition day of a Sentinel-2 image. For this, 21 images were obtained for the 5 months which were analysed. The SEBS interface was set up as shown in Figure 7, for retrieval of daily evapotranspiration.

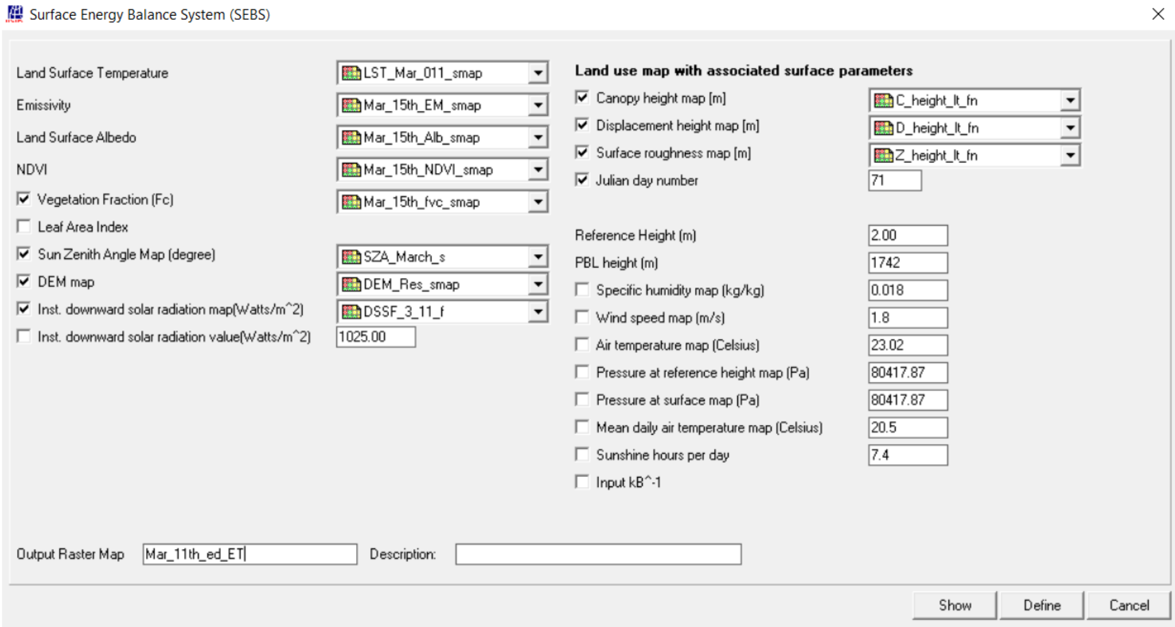

Figure 7: SEBS model set-up for retrieval of March 11th ET.

4.4.9. Retrieval of monthly evapotranspiration maps

To improve the temporal resolution of the SEBS derived evapotranspiration, the assumption of a constant and stable evaporative fraction was made. In a study, carried out in Naivasha, Farah et al. (2004) found that the evaporative fraction was fairly stable during the day, and especially at mid-day. To arrive at a relationship between the actual daily evapotranspiration and the average daily net radiation, inference was made to equation (4.14) cited in Muthuwatta, Ahmad, Bos, & Rientjes, (2010) and proposed by Bastiaanssen, Ahmad, & Chemin, (2002)

$$ET_{int} = \frac{dt * 86400 * 10^3}{\lambda \rho_w} \Lambda R_{n24t} \tag{4.14}$$

where ET_{int} is the total evapotranspiration for the number of days under consideration [mm], dt is the time interval in days, λ is the latent heat of vaporization [J Kg^{-1}], ρ_w is the density of water [Kg m^{-3}], Λ is the evaporative fraction and R_{n24t} is the average daily net radiation [W m-2]. From equation (4.14), the assumption that daily evapotranspiration is directly proportional to the average net radiation was made as show in equation (4.15) and (4.16)

$$ET_a = \kappa * R_n \tag{4.15}$$

$$\left(\frac{ET_a}{R_n}\right) = \kappa \tag{4.16}$$

where: κ is a constant proportional to the evaporative fraction. The actual evapotranspiration for the days where SEBS derived daily evapotranspiration were not available was obtained using equation (4.17).

$$ET_{ai} = \frac{ET_{a0}}{R_{n0}} * (R_{n1} + R_{n2} + R_{n3} \ldots + R_{ni}) \tag{4.17}$$

where ET_{ai} is the evapotranspiration for the days where SEBS derived evapotranspiration was not available [mm], ET_{a0} SEBS derived daily evapotranspiration for the closest acquisition day [mm], R_{n0} is the net radiation coinciding with the SEBS derived actual evapotranspiration and R_{n1} to R_{ni} are the average net radiation values for the subsequent days of integration [W m^{-2} s^{-1}]. Figure 8 was used to ascertain whether the assumption made in (4.16) was acceptable for the lower Catchment of Naivasha. It is a plot of the average daily net radiation against daily evapotranspiration; and shows that there is a correlation between the two, with an R^2 of 0.63. Figure 8 was derived using data for the months of April and May, because during this period the flux tower data was consistent, making it possible to derive latent heat flux, based on sensible heat flux and the Bowen ratio. This was not possible for the other days because the sonic anemometer was not functioning.

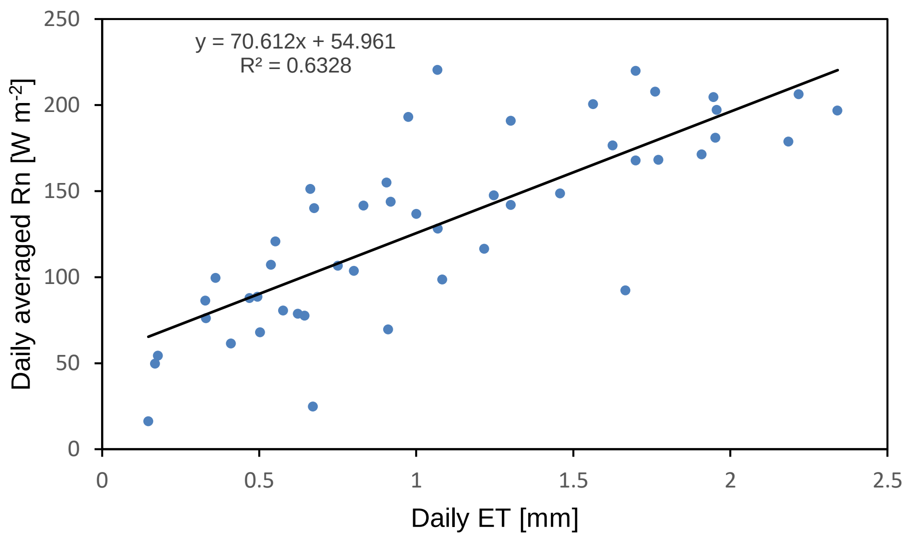

Figure 8: Correlation between flux tower net radiation and daily evapotranspiration.

4.5. Validation of SEBS evapotranspiration

The daily evapotranspiration maps derived in SEBS were validated using evapotranspiration data derived from the flux tower located at KWSTI and the Bowen ratio stations installed in Gorge farm. As a result, the flux tower data was used for validation of SEBS ET in non-irrigated pixels, while the Bowen ratio stations were used for validation of SEBS ET in the irrigated pixels. The comparison between SEBS-derived evapotranspiration and that derived from ground stations was done using the goodness of fit (R^2), as well as the Mean Absolute Error (MAE), Bias and the Root Mean Square Error (RMSE) using Equations (4.18), (4.19) and (4.20) respectively

$$MAE = \frac{\sum_{i=1}^{n}[abs(ET_{sebs,i} - X_{obs,i})]}{\sum_{i=1}^{n} ET_{obs,i}} \tag{4.18}$$

$$Bias = \frac{1}{n}\sum_{i=1}^{1} ET_{sebs,i} - \frac{1}{n}\sum_{i=1}^{n} ET_{obs,i} \tag{4.19}$$

$$RMSE = \sqrt{\frac{\sum_{i=1}^{n}(ET_{sebs,i} - ET_{obs,i})}{n}} \tag{4.20}$$

where $ET_{sebs,i}$[mm] and $ET_{obs,i}$[mm] are, the modelled and observed evapotranspiration respectively.

4.5.1. Flux tower derived evapotranspiration

The latent heat flux from the flux tower was calculated using the Bowen ratio method as shown in equation (4.21) and (4.22). A detailed discussion of these equations can be found in van der Velde, Su, Ek, Rodell, & Ma (2009) and Tol et al. (2015)

$$\lambda E = \frac{H}{\beta} \tag{4.21}$$

$$\lambda E = \frac{R_n - G_0}{1 + \beta} \tag{4.22}$$

where, λE is the latent heat flux, β is the Bowen ratio [-], and H is the sensible heat flux [W m^{-2}]. The energy balance closure was evaluated using latent heat obtained with equation (4.22), as shown in Figure 9.

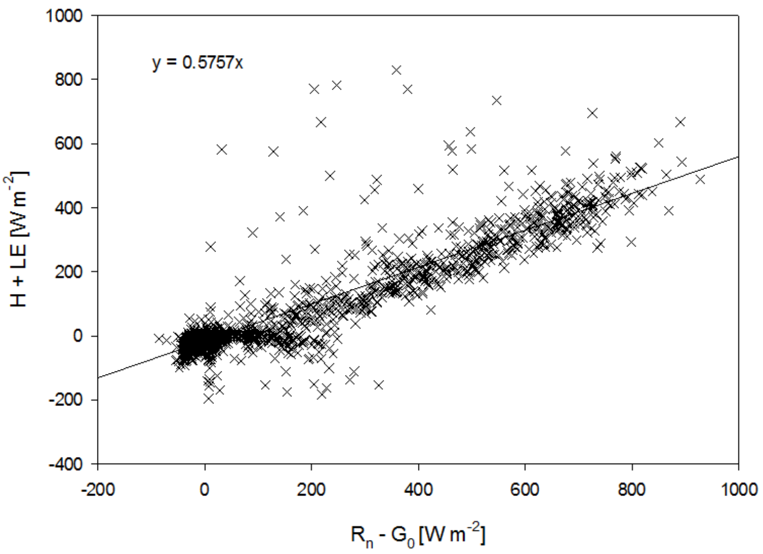

Figure 9: Energy balance closure analysis

Figure 9 shows that the flux tower has a closure error of about 42%, and this implies that the error would propagate to the validation results, if the tower data was used for validation as it is. According to Foken, (2008), the closure problem occurs due to underestimation of the turbulent fluxes or overestimation of the net radiation and the ground heat flux. This is mostly attributed to the mismatch between the source area of the upwelling radiation and the footprint of the turbulent fluxes (Foken, 2008). Given that equation (4.22) was going to be used for validation, it was necessary to have an understanding of the uncertainties that would propagate to the validation results. As a result, the latent heat flux obtained using equation (4.21) was corrected for closure using equation (4.23) proposed by (Zheng et al., 2014).

$$\lambda E_{cor} = \lambda E + Res * \frac{\lambda E}{\lambda E + H} \tag{4.23}$$

where λE_{cor} is the corrected latent heat flux [Wm^{-2}] and Res is the energy which is unaccounted for, obtained using equation (4.24).

$$Res = (R_n - G_0) - (H + \lambda E) \tag{4.24}$$

To get an understanding of the difference in derivation of evapotranspiration using equation (4.21), (4.22) and (4.23), a plot of daily evapotranspiration derived using the three methods was made. To achieve this flux tower data acquired between April and June 2016, when the sonic anemometer was working, was used and plotted as shown in Figure 10.

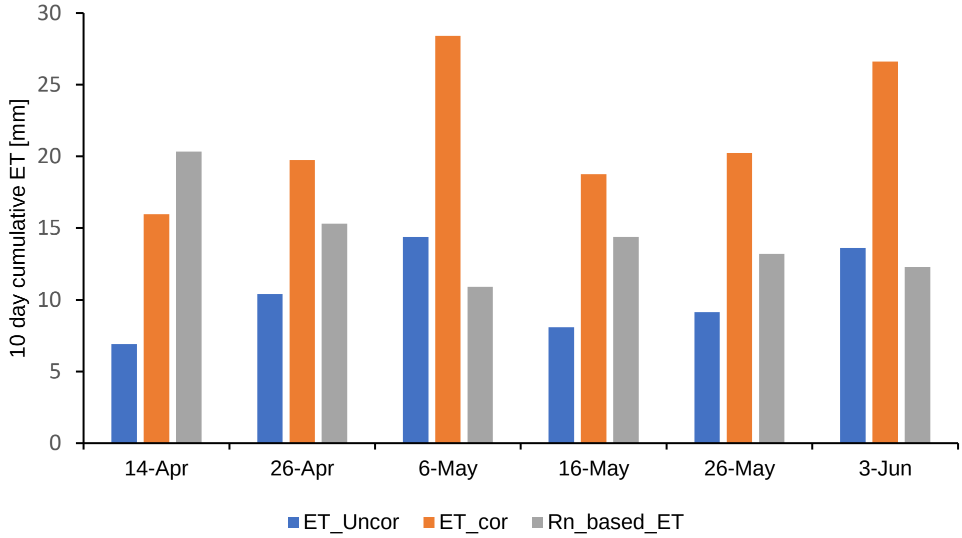

Figure 10: Comparison between the uncorrected H-based ET (ET_Uncor), the corrected H-based ET (ET_cor) and the net radiation-based ET

Figure 10, is a plot of 10 day cumulative ET_a for the period between 4th April and 3rd June, when sonic anemometer was operational. The variables in the figure correspond to:

- ET_Uncor refers to ET_a derived using Equation (4.21), that is, ET_a derived using the relation between sensible heat flux and Bowen ratio, without correcting for closure.
- ET_cor refers to ET_a derived using Equation (4.23), that is, ET_a derived using the relation between sensible heat and Bowen ratio after applying a correction factor.
- Rn_based_ET refers to ET_a derived using Equation (4.22), that is, ET_a derived using the relation between β, R_n and G_0.

Figure 10, show that the corrected sensible heat-based ET_a (ET_Cor) had generally higher daily evapotranspiration values; however, there were instances when Rn based ET_a (Rn_based_ET) overestimated evapotranspiration. While the available data constrained the study to the use of the Rn_based derived evapotranspiration, it is clear that the data used for validation generally underestimates the corrected sensible heat based evapotranspiration (ET_cor). This is best highlighted by Table 5, which shows a considerable difference in ET_a derived using the two methods.

Table 5: Error analysis comparing Rn_based ET_a to ET_cor (corrected sensible heat-based ET_a)

Error analysis	Rn_based ET_a proportion of the corrected ET_a
RMSE [mm]	1.68
MAE [mm]	1.3
Bias [mm]	0.76

4.5.2. Evapotranspiration derived from Bowen ratio stations

To validate the SEBS-derived evapotranspiration in the farms, two Bowen ratio stations were installed in Gorge farm within the pivots on 26th September 2016. These stations were installed in pivot PF3 located at coordinates S 00.84728°, E 036.38723° and pivot PB3 located at S 00.84471°, E 036.37867. It was not possible to use the stations to derive actual evapotranspiration because they lacked net radiation and soil heat flux sensors. However, by estimating the Bowen ratio, it was possible to validate the SEBS evaporative fraction. Furthermore, potential ET was also derived using Hargreaves equation in (4.25) proposed by Hargreaves, Asce, & Allen, (2003), and used to validate ET in the farms

$$ET_0 = 0.0023R_a(TC + 17.8)TR^{0.5} \tag{4.25}$$

where ET_0 [mm] is the reference evapotranspiration, R_a is the extra-terrestrial solar radiation [W m^{-2}], TR [˚C] is the difference between the daily maximum and minimum temperatures, and TC [˚C] is average of the minimum and maximum air temperature.

Bowen ratio and the evaporative fraction were computed using equations (4.26) and (4.27) discussed in detail by van der Velde et al. (2009)

$$\Lambda = \frac{1}{1+\beta} \tag{4.26}$$

$$\beta = \gamma \frac{T_{air1} - T_{air2}}{e_{air1} - e_{air2}} \tag{4.27}$$

Where, γ is the psychometric constant [Pa K^{-1}], T_{air1} and T_{air2} are the air temperatures at 2 m and 4 m height respectively; e_{air1} and e_{air2} are the actual vapor pressure as per measurements at 2 m and 4 m height respectively, Λ is the evaporative fraction [-], and β is the Bowen ratio.

4.6. CHIRPS Bias analysis and correction

As discussed in section 4.3.8, CHIRPS rainfall product was used in the computation of effective rainfall. In a previous study by Njuki, (2016), it was found that CHIRPS rainfall product performed better on a monthly time scale than on a daily time scale. It was therefore important to analyse the product for Bias before deriving a bias correction factor. The biases analysed were the Missed Bias (MB), Hit Bias (HB) and False Bias (FB), and they were evaluated according to definitions and equations (4.28), (4.29) and (4.30) by Habib, Haile, Tian, & Joyce (2012).

$$HB = \sum_{i=1}^{n} (R_{CHIRPS} - R_{gauge}) \,|(R_{CHIRPS} > 0 \& R_{gauge} > 0) \tag{4.28}$$

$$MB = \sum_{i=1}^{n} R_{gauge} \,|(R_{CHIRPS} = 0 \& R_{gauge} > 0) \tag{4.29}$$

$$FB = \sum_{i=1}^{n} (R_{CHIRPS} \,|(R_{CHIRPS} > 0 \& R_{gauge} = 0) \tag{4.30}$$

where: R is the precipitation, and n is the number of days.

The bias correction factor was computed using equation (4.31) proposed by Habib, Haile, Sazib, Zhang, & Rientjes, (2014)

$$BF_{TSV} = \left(\frac{\sum_{i=1}^{n} R_{CHIRPS,i}}{\sum_{i=1}^{n} R_{gauge}} \right) \tag{4.31}$$

where, BF_{TSV} is the time-space variant bias factor. The Bias factor was computed for the cumulative period where there was consistent data from four rainfall gauging stations located at close proximity to the farms. These stations are Nini Farm, Gorge Farm, Yacht and KWSTI. To achieve this, cumulative rainfall point maps were first created in ArcGIS. Using inverse distance weighted interpolation method implemented in python. Maps of four points corresponding to GPS points of the location of the four rainfall gauging stations were created, having the same spatial resolution and coordinate system as the CHIRPS product. The bias correction factor maps were obtained by dividing the cumulative January to June CHIRPS rainfall product by the cumulative gauge rainfall maps. This factor was then multiplied by the monthly CHIRPS rainfall maps to correct them for bias.

4.6.1. Computation of effective precipitation

Effective precipitation was computed by applying equation (4.32) proposed by van Eekelen et al., (2015) and adjusted by Njuki, (2016) to make it suitable for derivation of effective precipitation in irrigated areas,

$$P_{eff} = \left(\frac{E_{n,i}}{P_i} \right) * P_i \tag{4.32}$$

where $E_{n,i}$ is the monthly evapotranspiration from natural vegetation, whose effective rootzone depth is similar to that of crops grown in the farms, P_i is the monthly rainfall and P_{eff} is the effective precipitation.

4.6.2. Selection of natural land use classes

Njuki (2016) found that the effective rootzone of grass was more representative of the average effective root zone of crops grown in the farms in Naivasha. As a result, the natural land cover used to obtain evapotranspiration in a natural area was grass. This was obtained with the help of the landcover map in Figure 6 and GPS coordinates of natural land cover fields obtained during field work. As proposed by Njuki (2016), further filtering of the selected grass classes was necessary, to mask out the contribution of inflows from the saturated zones (lake and farms) into the natural land cover classes. An effective rainfall ratio was used in selecting the pixel corresponding to effective monthly precipitation. The logic behind the effective rainfall ratio is that effective precipitation should not exceed total precipitation received in that month. Njuki, (2016) stated that an effective rainfall range between 0.74 and 0.84 was acceptable. Consequently, this was the value range which was considered while selective pixels to retrieve effective precipitation. Equation (4.33) shows the equation used to derive the effective rainfall ratio

$$P_r = \left(\frac{E_{n,i}}{P_i} \right) \tag{4.33}$$

where, P_r is the effective rainfall ratio.

4.7. Computation of irrigation efficiency

Irrigation efficiency was calculated using the formulation of classical irrigation efficiency explained in section **Error! Reference source not found.**. However, Equation (2.13) was adjusted to Equation (4.34). This was done based on the reasoning that effective precipitation does not reduce the amount of irrigation water already consumed, but rather reduces the proportion of actual monthly ET resulting from irrigation

$$E_v = \frac{ET_a - P_{eff}}{W_g} \tag{4.34}$$

where, $(ET_a - P_{eff})$ represents the actual irrigation water consumption, that is, the amount of water supplied by irrigation used to meet the crop evapotranspiration needs; W_g is the actual irrigation water consumption and E_v is the irrigation efficiency.

The aridity index was computed using Equation (4.35) and was used in interpreting the irrigation efficiency results

$$A_m = \frac{P}{ET_0} \tag{4.35}$$

where, A_m is the monthly aridity index [-] and P is the monthly precipitation [mm]

5. RESULTS AND DISCUSSION

5.1. Downscaled land surface temperature

Land surface temperature was downscaled to the 10m Sentinel-2 resolution as discussed in Section 4.4.5. The total number of downscaled images was eighteen and they were used as inputs in SEBS for retrieval of actual evapotranspiration. Validation of the downscaled land surface temperature was not possible due to lack of in situ data, however, Figure 11 shows that the downscaled images depict more detail in the study area than the original images. Moreover, some features like the farms and catchment contours are more visible in the downscaled image.

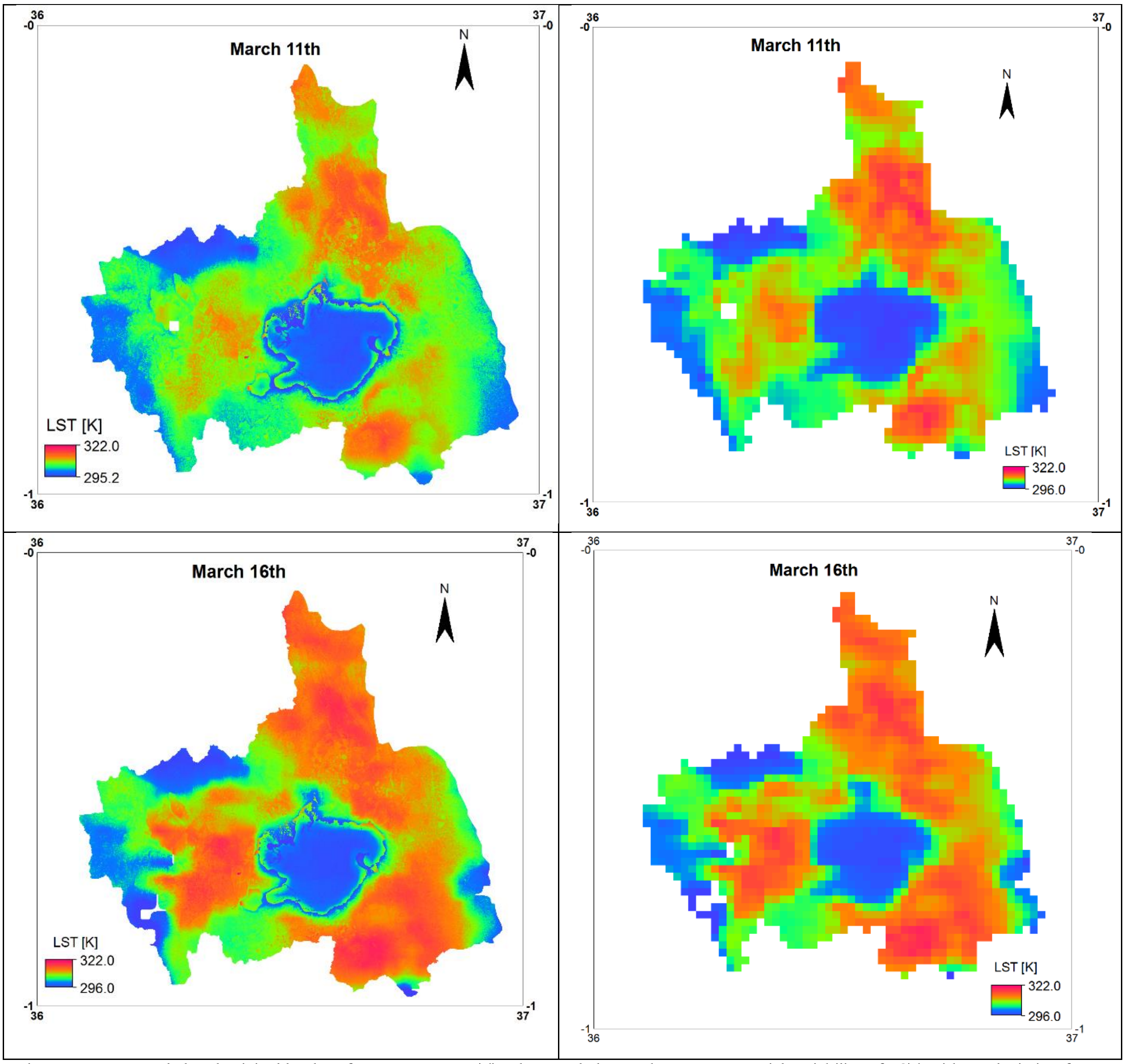

Figure 11: Downscaled and original land surface temperature. The downscaled map shows more spatial variability of LST, without deviating from the maximum and minimum temperature-range of the original the image by a large margin.

The difference in minimum and maximum temperature between the downscaled and the original image was found to be within 3K, which is as a result of un mixing of the aggregated coarse resolution LST. The downscaled image looks acceptable for most of the land surface features, and depicts the land surface temperature pattern seen in the coarse resolution image. However, the downscaling procedure seems to introduce some artefacts at the interface between the lake shore and land. Patches of high land surface temperatures are visible at the shore of the lake, attributed to the sand at the beach which gets heated fast during the day. Moreover, some of these artefacts show the difficulty of downscaling land surface temperatures at such an interface because of the sharp NDVI contrast between the lake and the riparian land. This could be because the downscaling algorithm does not factor the NDVI of water bodies.

5.2. Evapotranspiration

Evapotranspiration was calculated at a daily scale in SEBS and aggregated to monthly after gap filling, making it possible to compute irrigation efficiency.

5.2.1. SEBS model sensitivity

A study by van der Kwast et al. (2009) found SEBS to be less sensitive to most of the satellite derived inputs like the vegetation indices and albedo. This is because sensible heat flux is more dependent on land surface temperature and the other meteorological parameters obtained at the reference height (van der Kwast et al., 2009). As a result, the sensitivity analysis was carried out with a bias on the meteorological parameters.

The sensitivity of SEBS was analysed by varying the inputs by a range of ± 20% at 10% interval, with the exception of air temperature. For air temperature, deviations of ± 3K were used, at an interval of 1.5 K, because 2 K is the recommended accuracy for the physical parameter in SEBS (Z. Su, 2002). Sensitivity was thus computed for negative or positive deviation from the measured inputs as proposed by van der Kwast et al., (2009), using equation (5.1)

$$S_i(ET_\pm) = \left(\frac{ET_\pm - ET_0}{ET_0}\right) * 100 \tag{5.1}$$

where S_i is the sensitivity of the inputs; ET_+, ET_- and ET_0 are the derived evapotranspiration values when the input is varied by 20%, -20%, and when it is equal to the reference value, respectively. This is with exception of air temperature which is varied by ± 3K.

The sensitivity analysis results in Figure 12 generally agree with findings by van der Kwast et al. (2009) because it was found to be generally less sensitive to most of the parameters which were evaluated (sensitivity <10%). It was also consistent with findings by Z. Su, (2002) who pointed out that it is very sensitive to air temperature variations, and proposed that the accuracy of the temperature should be within 2 K. In agreement with this, the model was found to be approximately 15% sensitive to air temperature variations as shown in Figure 12. Moreover Figure 12 shows that the model is reasonably sensitive to the Downward Shortwave Surface Flux (DSSF) and sunshine hours. This is realistic because DSSF and sunshine hours are interrelated, in that the lack of sunshine hours, limits DSSF. On the other hand, DSSF affects air and land surface temperature directly.

The retrieval of evapotranspiration in SEBS assumed a constant value of air temperature. This can introduce significant errors in the calculated evapotranspiration given that SEBS is very sensitive to air temperature. To ascertain the impact of using air temperature measurements from the flux tower to be representative of the lower basin, an analysis of diurnal variation in temperature was carried out. In this, corresponding air temperatures at 2m height measured at the flux tower, and the Bowen ratio stations were compared.

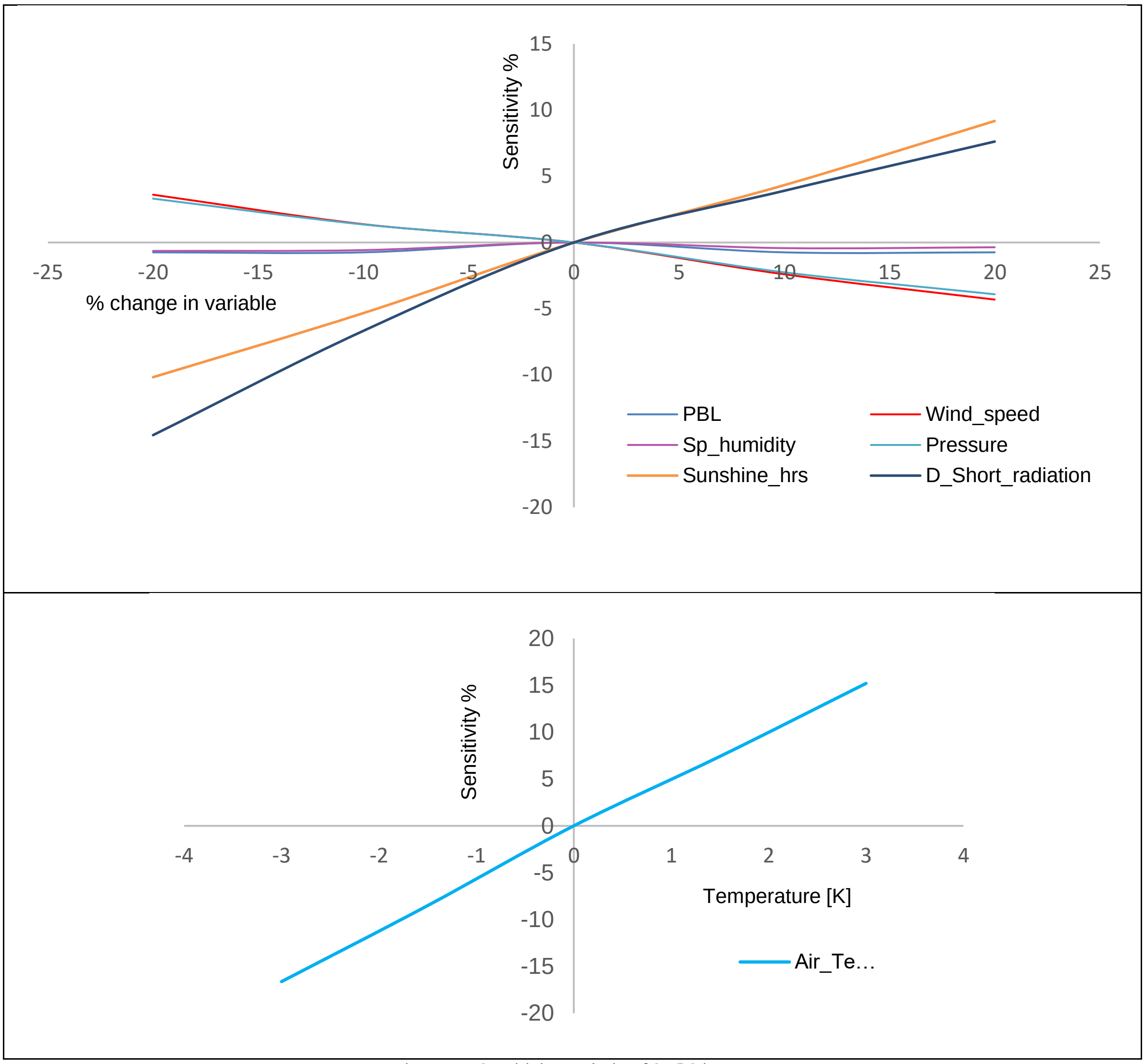

Figure 12: Sensitivity analysis of SEBS inputs

Figure 13 shows the comparison between air temperature measurements at Gorge farm and KWSTI during the sunshine hours, that is 6:30 to 18:30 measured between 27th September and 3rd of October. It is a comparison of the diurnal variation in air temperature between the flux tower and the Bowen ratio station for measurements taken at 2 m height using the two equipment, and for the days under consideration.

The standard deviation analysis show that on average, the difference in temperature between the farms and KWSTI, where the flux tower is located could be up to 2K as shown in Table 6, which is acceptable according to Z. Su (2002). It is worth noting that the standard deviation represents the overall situation. Figure 13 shows that there are instances when the difference in air temperature at the farm and at KWSTI exceeds 3K. From Figure 12, we find that when the air temperature varies by more than 3 K, the derived ET_a can be over/underestimated by more than 15%. At such conditions, the assumption that air temperature is constant is not valid, and leads to errors in the calculated evapotranspiration.

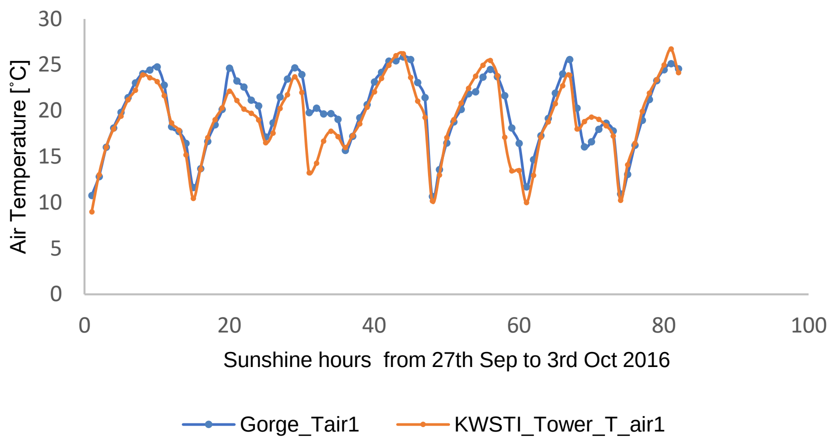

Figure 13: Comparison between air temperature at Gorge farm and KWSTI

Table 6: Variation of air temperature between Gorge farm and KWSTI

Statistical analysis	Gorge farm air temperature vs KWSTI
Standard deviation	1.9

5.2.2. Validation of SEBS derived evapotranspiration

The flux tower climatology footprint for the year 2012 to 2014, Figure 14, was used to obtain representative values of SEBS derived evapotranspiration for validation. The flux tower climatology footprint was derived according to Kljun, Calanca, Rotach, & Schmid (2015), and was used under the assumption that it was representative of the general source area of fluxes for the KWSTI flux tower.

The use of the footprint was made with the assumption that only pixels within the footprint contributed to the evapotranspiration value measured by the flux tower. The footprint values are transfer functions for the variables being measured at the surface, in this case evapotranspiration (Kljun et al., 2015). As a result, the footprint values are weights for the transfer of evapotranspiration from the corresponding SEBS ET pixels to the point where the flux measurements are taken, that is the flux tower. However, this statement is only true if the values of the footprint add up to one.

To retrieve the SEBS ET value corresponding to the flux tower measurement, the 80% footprint source area was first masked out as shown in Figure 14. This is because it represents the area with the largest weight on the measured fluxes, especially in unstable conditions when vertical advection is highest. The masked footprint was then resampled to the resolution of the SEBS ET maps. This was obtained by multiplying SEBS ET with flux tower foot print, and then dividing the result with the sum of the value of flux tower foot print. The result was taken as the representative SEBS ET measurement corresponding to the flux tower measurement for that day.

The use of the climatology flux tower foot print was used with the assumption that it generally represents the source area of fluxes. While this is true over a longer timescale like a year, it is not valid at a daily timescale because the foot print is affected by the wind direction; and thus, the measured fluxes depends on the dominant wind direction for that day. This could have also contributed to the mismatch between the measured and observed evapotranspiration in the validation data. While it would have been more practical to use a daily footprint, this was not possible because of the challenges with the sonic anemometer.

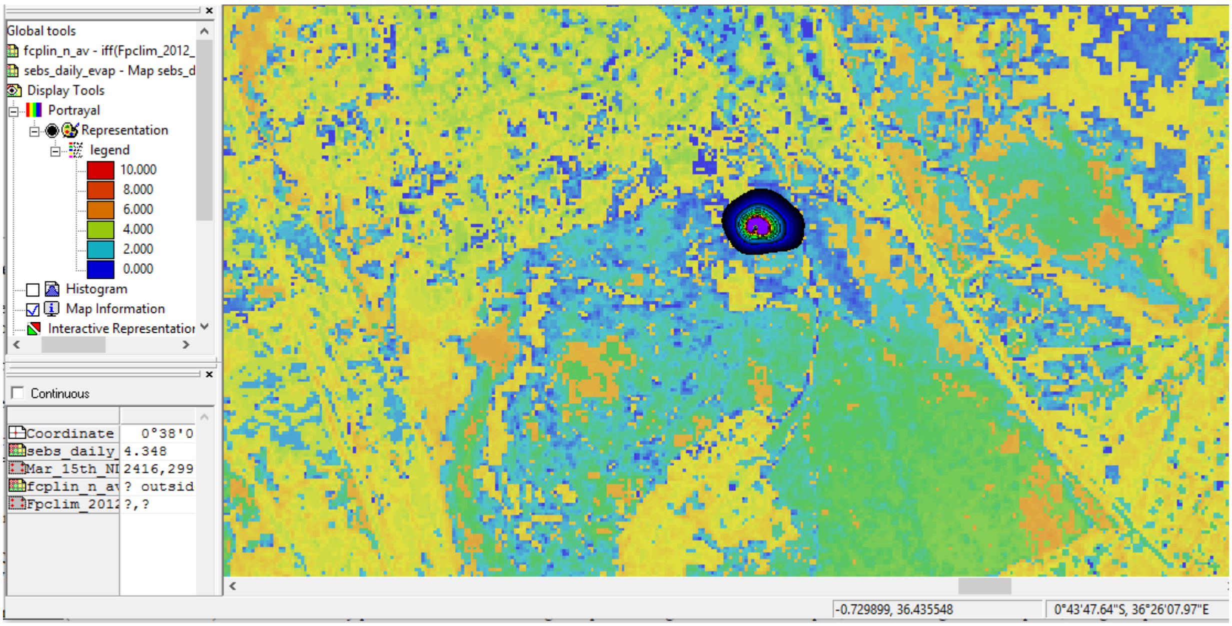

Figure 14: Flux tower foot print showing the 80% source area

5.2.3. Validation of SEBS evapotranspiration over non-irrigated pixels

Figure 15 shows that SEBS overestimated evapotranspiration in the non-irrigated areas, which is evident in that all the SEBS ET measurements lie above the one to one line. While the figure shows an acceptable R^2, the magnitude of ET overestimation was not anticipated; considering a previous study by Njuki (2016) showed acceptable performance of SEBS in the same area.

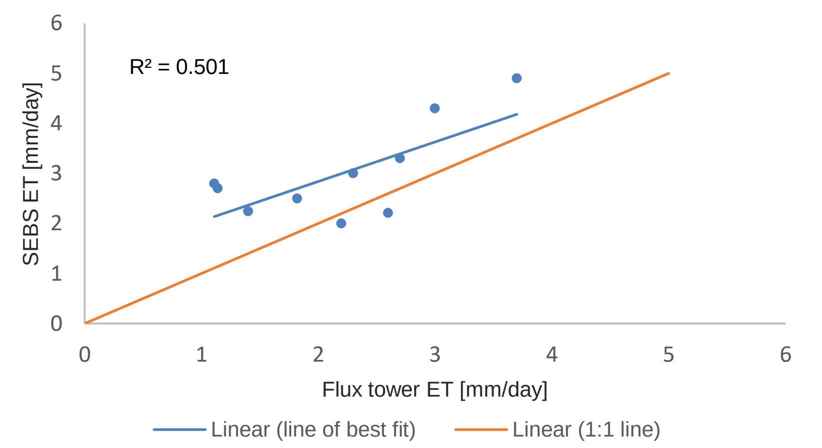

Figure 15: Validation of SEBS ET over non-irrigated areas

Table 7: Validation of SEBS ET over Savannah vegetation

Analysis of validation results	Flux tower
MAE [mm]	0.9
RMSE [mm]	1.03
Bias [mm]	0.798
R^2	0.5

The main reason for the overestimation is implied in Figure 10, which shows that ET derived using equation (4.22), (Rn_based ET), is generally less than the corrected H-based ET (ET_cor) in equation (4.23). According to Foken (2008), overestimation of the net radiation and ground heat flux is sighted as one of the main reasons contributing to lack of energy balance closure. Given that the ET_a used for validation was derived using equation (4.22), reliant on the difference between net radiation and ground heat flux; it leads to the conclusion that the flux tower is overestimating ground heat flux. In addition, surface energy balance models have been generally found to overestimate ET_a in water limited areas as stated by Gökmen (2013). These two uncertainties explain why the validation results show that SEBS overestimated evapotranspiration in the Savannah. The values of RMSE, MAE, and bias in

Table 7 are within those in Table 5. This implies that the overestimation of evapotranspiration is most likely due to the method used to derive the validation data.

5.2.4. Validation over irrigated pixels

Validation over irrigated pixels was carried out in two steps. First the Hargreaves method was used to derive reference ET using the temperature data from the Bowen ratio stations. The reference ET was then converted to potential ET by multiplying it with the crop coefficient (K_c). The assumption made in using this method is that in the irrigated areas, ET_a is equal ET_p and consequent, the air temperature is equal to the potential temperature. The crop factors were obtained from FAO (2007), and were extracted corresponding to the crops which were in pivots PB3 and PF3, where the two stations were installed.

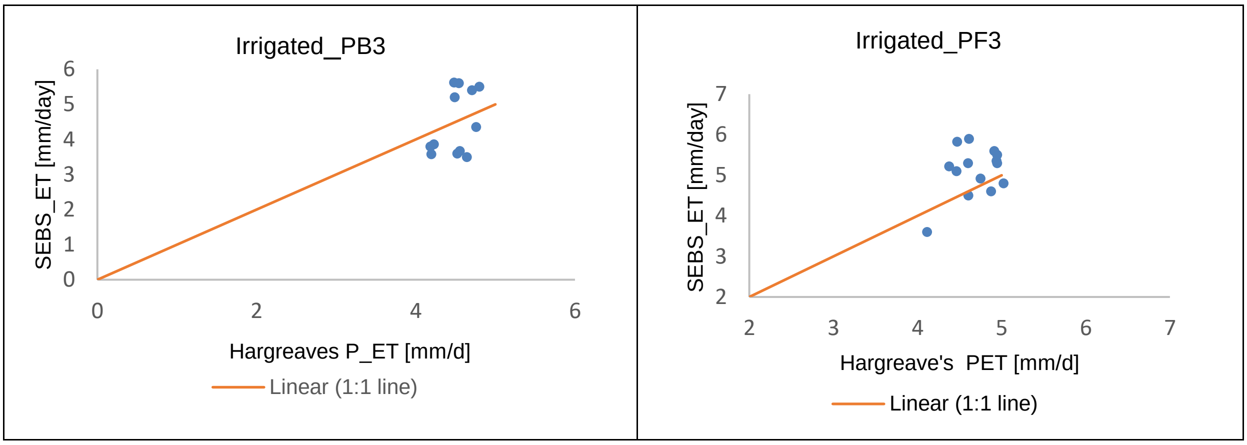

Figure 16: Validation of SEBS-ET in the irrigated area using Hargreaves ET_p obtained by multiplying Hargreaves ET_0 by K_c

From Figure 16, it was observed that the range within which SEBS derived ET_a was varying with respect to the Hargreaves derived ET_p was very small; consequently, a trendline was not considered necessary. From the RMSE, the performance of SEBS over irrigated areas looks acceptable given that the largest deviation is about 0.8 mm, with a bias less than 0.5 mm, as shown in

Table 8. The overall performance of SEBS over the irrigated areas shown in Figure 16, is better than in the non-irrigated areas, Figure 15.

Table 8: Statistical analysis on the performance of SEBS in the irrigated areas.

Statistical analysis	Pivot B3 (Broccoli)	Pivot F3 (Fine beans)
RMSE [mm]	0.8	0.68
MAE [mm]	0.71	0.83
Bias [mm]	-0.04	0.42

To confirm whether the performance of SEBS over the irrigated areas was reasonably acceptable, validation was done for the SEBS evaporative fraction, using Bowen ratio derived from the stations, as described in section 4.5.2. Figure 17 shows that SEBS evaporative fraction had a good correlation with the evaporative fraction measured at the Bowen ratio stations at the time of overpass. The RMSE, MAE and bias indicate that SEBS estimate of evaporative fraction closely matched, that measured by the Bowen ratio stations. Given that SEBS-derived ET is directly proportional to the evaporative fraction it follows that the performance of SEBS over the irrigated areas was acceptable, based on the validation results in Table 9.

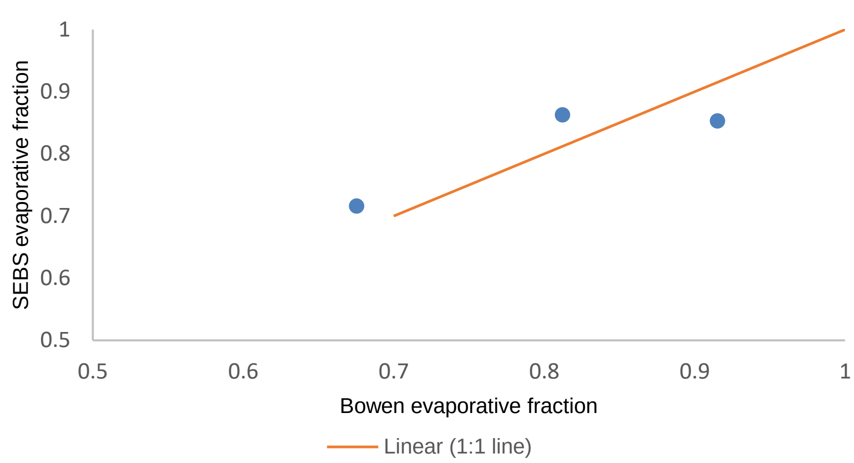

Figure 17: Validation of SEBS using evaporative fraction

Figure 17 shows that there were no enough SEBS-derived ET images at the satellite overpass to use for validation. This is because collection of validation data using the Bowen ratio stations started on 26th September 2016, during fieldwork. Despite this, large deviations of evapotranspiration are not expected in the irrigated areas, because they are rarely under water stress. The statistical analysis show that the RMSE in the evaporative fraction is less than 0.05, implying that the satellite is measuring almost the same value of evaporative fraction as the Bowen stations at the time of overpass. The bias on the other hand is almost negligible that is -0.01.

Table 9: Validation of SEBS evaporative fraction using Bowen ratio stations

Statistical analysis of EF	Evaporative fraction
RMSE [-]	0.05
MAE [-]	0.05
Bias [-]	-0.01

5.3. SEBS monthly evapotranspiration

The monthly evapotranspiration maps were retrieved as discussed in Sub-section 4.4.9, where the net radiation from ECMWF was used to improve the temporal resolution of the derived ET maps. Figure 18 shows that the ET maps reflect the seasonality the area to some extent, with the exception of February. This is because in February, the SEBS-derived ET maps used for gap filling in were few and concentrated towards the end of the month, when the March to May rainy season was just beginning. As a result, the February ET map does not clearly depict the seasonality of ET in non-irrigated areas, that is less ET is expected in the non-irrigated areas.

Figure 18 shows that almost all the farm area is irrigated in the months of October and September, as compared to January, February and March. This could explain why Njuki, (2016) found that Gorge farm had lower efficiency in August and September 2014 as compared to the other months. It could be that the less irrigation water consumption between January to March is as a result of less area being irrigated as compared to the period around September.

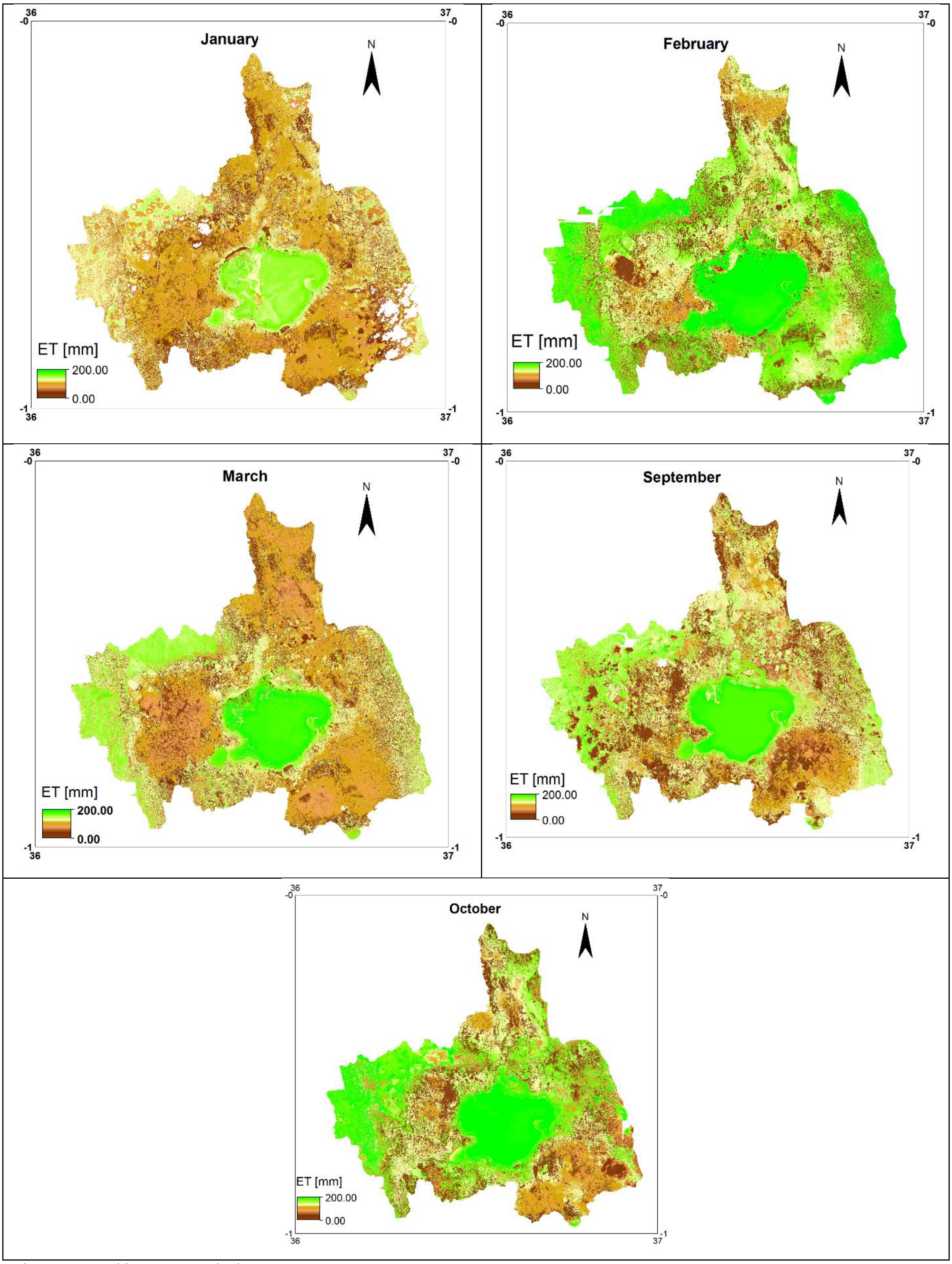

Figure 18: Monthly evapotranspiration maps.

5.4. Computation of irrigation efficiency

Irrigation efficiency was calculated for Gorge farm and FHK Kingfisher Veg farm as discussed in section 4.7. The difference between the evapotranspiration maps of the respective farms and the effective precipitation was used to compute irrigation efficiency, by dividing it with the monthly irrigation water consumption.

5.4.1. Analysis of CHIRPS precipitation

Precipitation from four stations was used to correct CHIRPS rainfall product for bias, for the period when there was data from both the respective gauge and CHIRPS product. The performance of CHIRPS was consistent with previous findings by Njuki, (2016), where he found the product to poorly match the gauge measurements on a daily timescale. The biases can be deduced from the graphs in Figure 19, where the points that lie along x axis represent the missed bias of the CHIRPS product; those that lie along the y axis represent the false bias, while those that lie above the axes, but still outside the one to one line, indicate the hit bias of the product.

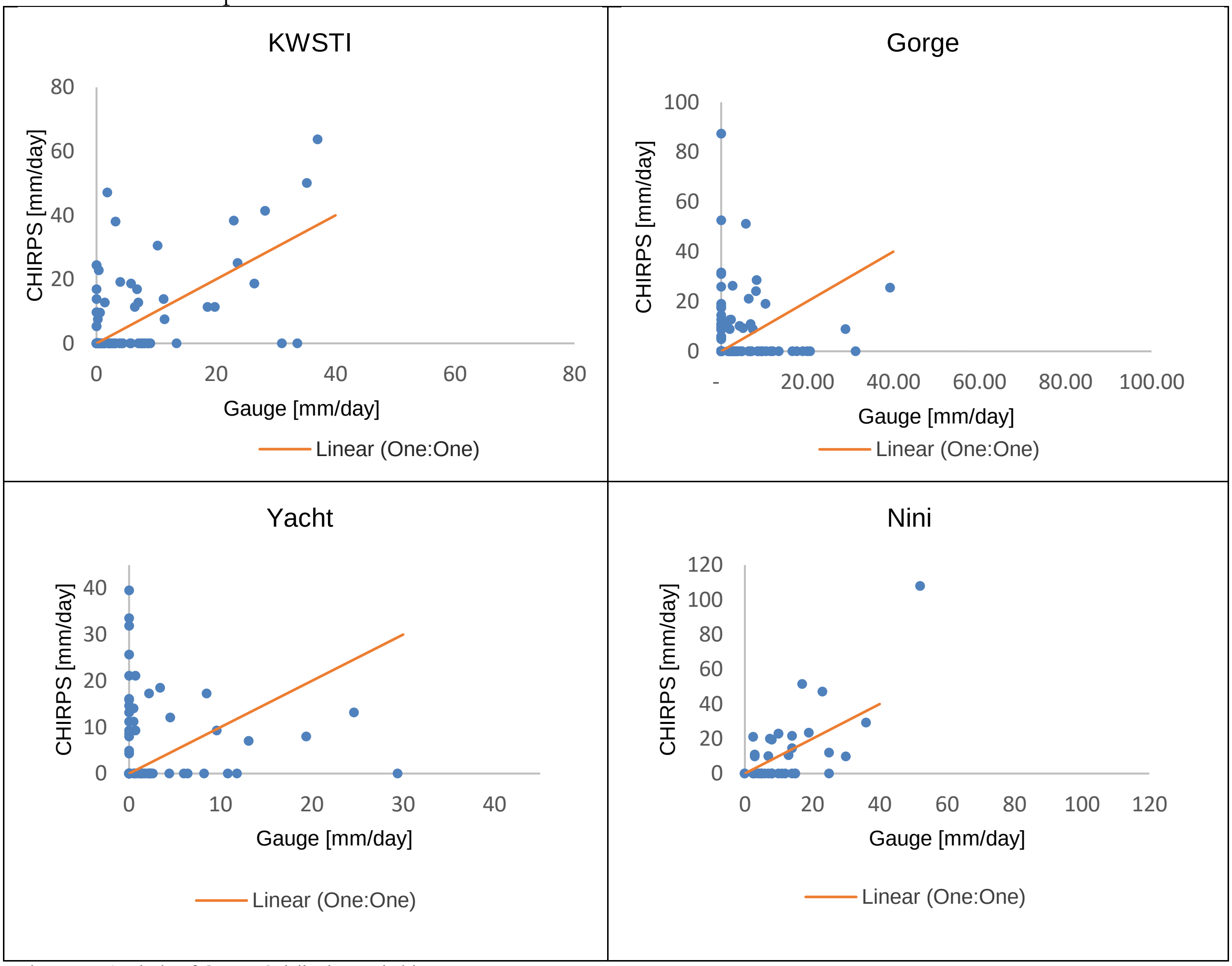

Figure 19: Analysis of CHIRPS daily timescale bias

The analysis of daily biases Table 10 confirms the poor performance of CHIRPS at a daily timescale, with the measurements corresponding to the Gorge station having the largest bias.

Table 10 Performance of CHIRPS product at a daily timescale

Statistical analysis	KWSTI	Nini	Yacht	Gorge
Hit bias [mm]	239.7	184.9	79.9	147.7
False bias [mm]	273.2	253.4	102.1	290.6
Miss bias [mm]	122.09	190.5	248.5	380

At a monthly timescale, the performance of CHIRPS product was found to significantly improve, with the largest bias being around 31 mm as shown in Table 11. Figure 20 also shows that most of the miss and false biases compensate for each other at a monthly time scale, with the hit bias being the most predominant. These analyses show the necessity of applying a bias correction factor before using the CHIRPS data to derive effective precipitation.

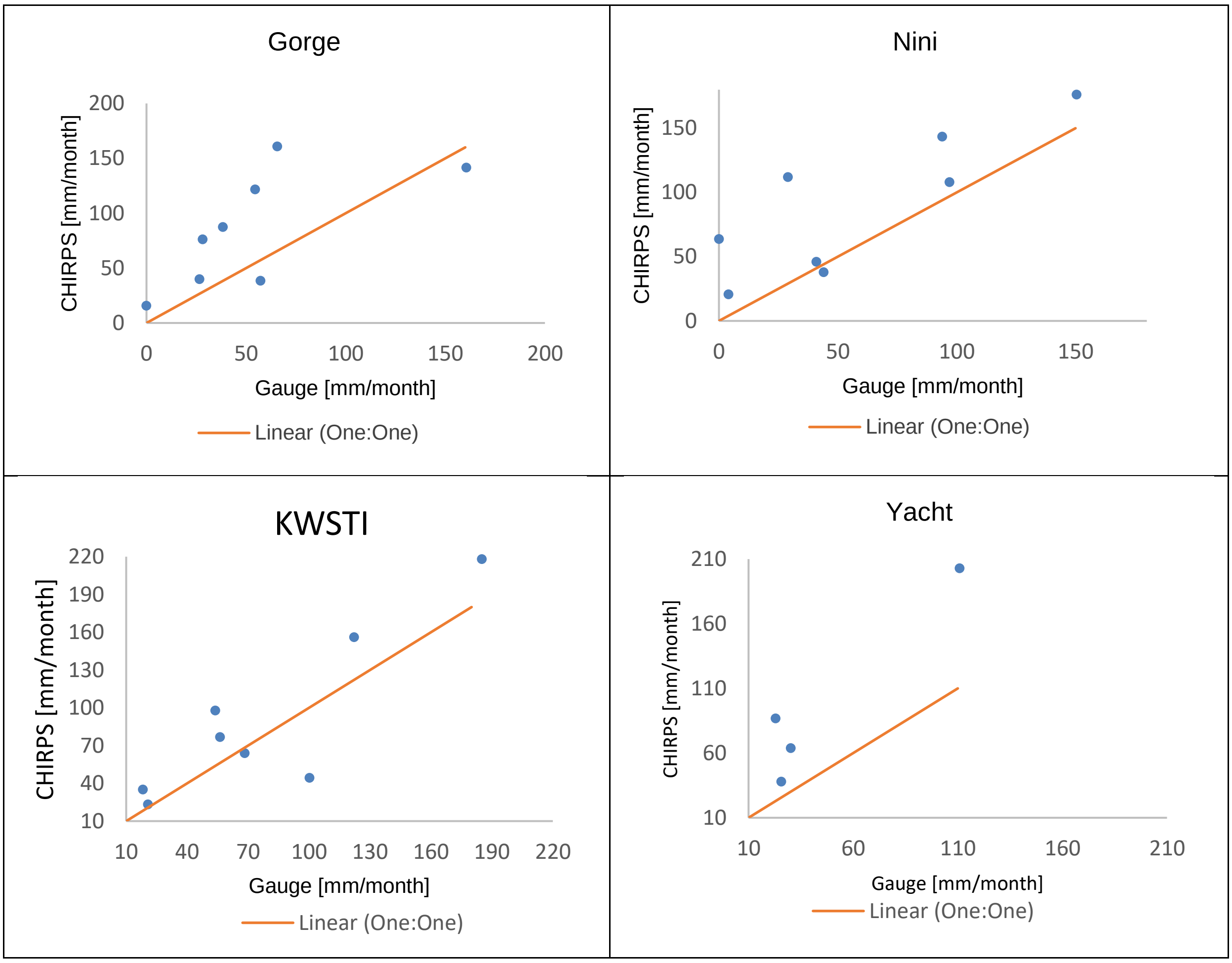

Figure 20: Monthly analysis of CHIRPS rainfall product bias

Table 11 Performance of CHIRPS at a monthly time scale

Station name	Bias [mm]	RMSE [mm]	MAE [mm]
Yacht Club	25.12	50.25	58.63
KWSTI	11.2	31.6	26.3
Nini	30.9	42.6	32.5
Gorge	31.23	40.7	49.21

5.4.2. Irrigation water consumption

To compute irrigation efficiency, the irrigation water consumption was first computed as explained in Section 4.7, and using equation (5.2)

$$ET_{irr} = ET_a - P_{eff} \tag{5.2}$$

where, ET_{irr} is the actual irrigation water consumption as computed using remote sensing.

Table 12 Summary of irrigation water consumption

Month	Gorge farm consumption [m³]	FHK Kingfisher farm consumption [m³]
January	121041	23069
Feb	494703	98382
March	430265	81504
September	247493	
October	273833	

The overall irrigation water consumption of Gorge farm is higher than Finlays. This is because the area under irrigation in Gorge farm is almost four times that of Finlays as shown in Section 4.1. The irrigation efficiency was obtained by dividing the irrigation consumption with the gross water abstraction by the farms as shown in Equation (4.34). Table 13 shows that Gorge farm irrigation systems/practices are more efficient than those of Kingfisher farm. The efficiency of Gorge farm appears to be more sensitive to the aridity index as shown in Figure 21.

Table 13: Breakdown of irrigation efficiency

Month	Gorge farm irrigation efficiency %	FHK Kingfirsher Veg Farm irrigation efficiency %	Aridity Index
January	62.2	32.5	0.46
Feb	100	53	0.44
March	99.1	50	0.2
September	53		0.8
October	81		0.47
Overall efficiency	77.4	45	

The analysis of irrigation efficiency was found to agree with findings by Njuki (2016) that the irrigation efficiency of Gorge seems to be lowest in the month of September even with the high aridity index experienced in the month as shown Figure 21. This implies that soil moisture data is not factored in irrigation scheduling as Njuki (2016) concluded.

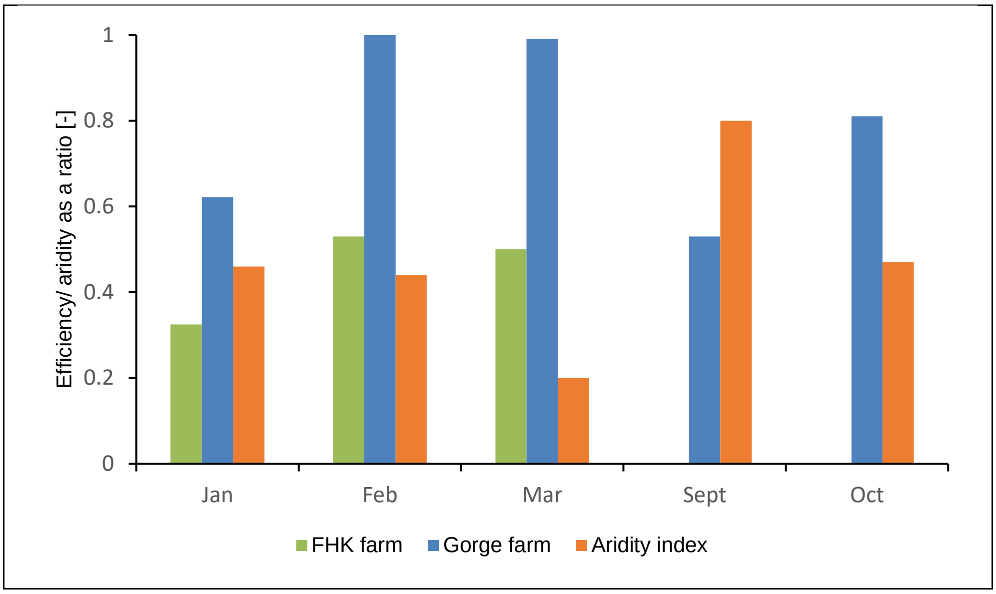

Figure 21: Analysis of correlation between irrigation efficiency and aridity index

6. CONCLUSION AND RECOMMENDATIONS

6.1. Conclusion

The initial objective of this research was to estimate irrigation efficiency of open irrigated farms using Sentinel-2 and 3 data. However, Sentinel-3 data was replaced with MODIS land surface temperature because of delays in dissemination of Sentinel-3 data. Irrigation efficiency was thus retrieved at 10 m spatial resolution using Sentinel-2 and MODIS land surface temperature. The study shows that Sentinel-2 and downscaled MODIS land surface temperature can be used to derive high resolution actual evapotranspiration maps.

MODIS LST was downscaled to the 10 m resolution of Sentinel-2, using thermal sharpening procedure. There was no data to validate the accuracy of the downscaling, however, the downscaled images seem to capture the LST pattern in the coarse resolution image as shown in Figure 11; while at the same time, showing more detail of the study area.

Evapotranspiration maps were derived in SEBS, and using the gap filling procedure in Equation (4.17), it was aggregated to monthly ET_a as shown in Figure 18. The validation of the 10 m resolution SEBS ET_a showed that it performed better in the irrigated areas than in the non-irrigated areas. The RMSE range over the irrigated areas was between 0.8 and 0.05 mm and Table 9 and Table 10 respectively, while over the non-irrigated area, the RMSE was about 1mm.

The monthly evapotranspiration maps seem to depict the seasonality of the area with the exception of February. From Figure 18, the months of January and March show lower evapotranspiration over the Savannah as compared to September and October.

From Table 13, it is implied that efficiency of open irrigated farms in the lower Catchment of Naivasha varies from farm to farm. This is so because the overall irrigation efficiency of Gorge farm was found to be around 77%, while that of FHK Kingfisher farm was 45%. This is expected because the two farms use different irrigation systems, and thus it could indicate that Gorge farm has better irrigation systems and practices as compared to Kingfisher.

Comparison between the irrigation efficiency and the aridity index does not give very conclusive information, however for Gorge farm it seems that the irrigation efficiency decreases with an increase in aridity. This is consistent with findings by Njuki (2016).

6.2. Recommendations

Sentinel-2 should be used in combination Landsat 8 images (higher spatial-temporal resolution) and LST derived from MODIS and Sentinel-3, to derive monthly and annual ET; without using the gap filling procedure in Equation (4.17) or the reference ET method applied by Njuki (2016).

Subsequent studies should be carried out with complete annual data, both satellite and validation data, to be able to capture the seasonal variability of evapotranspiration.

A more detailed and representative land use ad land cover map should be made for the Naivasha Catchment area at the 10 m spatial resolution of Sentinel-2, and validated.

The downscaled land surface temperature maps should be validated for the study area.

LIST OF REFERENCES

Abdul Karim, S. N. A., Ahmed, S. A., Nischitha, V., Bhatt, S., Kiran Raj, S., & Chandrashekarappa, K. N. (2013). FAO 56 Model and Remote Sensing for the Estimation of Crop-Water Requirement in Main Branch Canal of the Bhadra Command area, Karnataka State. *Journal of the Indian Society of Remote Sensing*, *41*(4), 883–894. https://doi.org/10.1007/s12524-012-0238-z

Akdim, N., Alfieri, S., Habib, A., Choukri, A., Cheruiyot, E., Labbassi, K., & Menenti, M. (2014). Monitoring of Irrigation Schemes by Remote Sensing: Phenology versus Retrieval of Biophysical Variables. *Remote Sensing*, *6*(6), 5815–5851. https://doi.org/10.3390/rs6065815

Allen, R. G., Pereira, L. S., Raes, D., & Smith, M. (1998). Crop evapotranspiration -Guidelines for computing crop water requirements -FAO Irrigation and drainage paper 56.

Awange, J. L., Forootan, E., Kusche, J., Kiema, J. B. K., Omondi, P. A., Heck, B., … Gonçalves, R. M. (2013). Understanding the decline of water storage across the Ramser-Lake Naivasha using satellite-based methods. *Advances in Water Resources*, *60*, 7–23. https://doi.org/10.1016/j.advwatres.2013.07.002

Bastiaanssen, W. G. M., Ahmad, M.-D., & Chemin, Y. (2002). Satellite surveillance of evaporative depletion across the Indus Basin. *Water Resources Research*, *38*(12), 9-1-9–9. https://doi.org/10.1029/2001WR000386

Becht, R., & Harper, D. M. (2002). Towards an understanding of human impact upon the hydrology of Lake Naivasha, Kenya. *Hydrobiologia*, *488*, 1–11. https://doi.org/10.1023/A:1023318007715

Bhattarai, N., Shaw, S. B., Quackenbush, L. J., & Im, J. (2016). International Journal of Applied Earth Observation and Geoinformation Evaluating five remote sensing based single-source surface energy balance models for estimating daily evapotranspiration in a humid subtropical climate. *International Journal of Applied Earth Observations and Geoinformation*, *49*, 75–86. https://doi.org/10.1016/j.jag.2016.01.010

Brutsaert, W. (2005). *Hydrology : an introduction*. Cambridge University Press.

Chauhan, S., & Shrivastava, R. K. (2009). Performance Evaluation of Reference Evapotranspiration Estimation Using Climate Based Methods and Artificial Neural Networks. *Water Resources Management*, *23*(5), 825–837. https://doi.org/10.1007/s11269-008-9301-5

Dee, D. P., Uppala, S. M., Simmons, A. J., Berrisford, P., Poli, P., Kobayashi, S., … Rosnay, de P. (2011). The ERA-Interim reanalysis: configuration and performance of the data assimilation system. *Quarterly Journal of the Royal Meteorological Society Q. J. R. Meteorol. Soc*, *137*, 553–597. https://doi.org/10.1002/qj.828

Dembélé, M., & Zwart, S. J. (2016). Evaluation and comparison of satellite-based rainfall products in Burkina Faso, West Africa. *International Journal of Remote Sensing*, *37*(17), 3995–4014. https://doi.org/10.1080/01431161.2016.1207258

ESA. (2015). SENTINEL-2 User Handbook, (1), 64. https://doi.org/GMES-S1OP-EOPG-TN-13-0001

FAO. (2003). Unlocking the Water Potential of Agriculture. Retrieved from http://www.fao.org/3/a-y4525e/index.html

FAO: Food and Agriculture Organization of the United Nations. (2007). Chapter 6 - ETc - Single crop coefficient (Kc). Retrieved February 7, 2017, from http://www.fao.org/docrep/X0490E/x0490e0b.htm

Farah, H. O., Bastiaanssen, W. G. M., & Feddes, R. A. (2004). Evaluation of the temporal variability of the evaporative fraction in a tropical watershed. *International Journal of Applied Earth Observation and Geoinformation*, *5*(2), 129–140. https://doi.org/10.1016/j.jag.2004.01.003

Farr, T. G., Rosen, P. A., Caro, E., Crippen, R., Duren, R., Hensley, S., … Alsdorf, D. (2007). The Shuttle Radar Topography Mission. *Reviews of Geophysics*, *45*(2), RG2004. https://doi.org/10.1029/2005RG000183

Feng, G., Cobb, S., Abdo, Z., Fisher, D. K., Ouyang, Y., Adeli, A., & Jenkins, J. N. (2016). Trend analysis and forecast of precipitation, reference evapotranspiration and rainfall deficit in the Blackland Prairie of Eastern Mississippi. *Journal of Applied Meteorology and Climatology*, JAMC-D-15-0265.1. https://doi.org/10.1175/JAMC-D-15-0265.1

Foken, T. (2008). the Energy Balance Closure Problem: an Overview. *Ecological Applications*, *18*(6), 1351–1367. https://doi.org/10.1890/06-0922.1

Funk, C., Peterson, P., Landsfeld, M., Pedreros, D., Verdin, J., Shukla, S., … Washington, R. (2015). The climate hazards infrared precipitation with stations—a new environmental record for monitoring

extremes. *Scientific Data*, *2*, 150066. https://doi.org/10.1038/sdata.2015.66
Gökmen, M. (2013). Earth Observation For Quantifying Ecohydrological Fluxes and Inter-Relations: A Regional Case – The Konya Closed Basin, Turkey. Doctoral Thesis. University of Twente, Faculty of Geo-information Science and Observation (ITC).
Gokmen, M., Vekerdy, Z., Lubczynski, M. W., Timmermans, J., Batelaan, O., & Verhoef, W. (2013). Assessing Groundwater Storage Changes Using Remote Sensing–Based Evapotranspiration and Precipitation at a Large Semiarid Basin Scale. *Journal of Hydrometeorology*, *14*(6), 1733–1753. https://doi.org/10.1175/JHM-D-12-0156.1
Granell, C., Casteleyn, S., & Atzberger, C. (2015). Editorial: Geospatial Data Capturing, Processing, Analysis, and Visualization in Agro-Geoinformatics. *Frontiers in Environmental Science*, *3*. https://doi.org/10.3389/fenvs.2015.00076
Habib, E., Haile, A., Sazib, N., Zhang, Y., & Rientjes, T. (2014). Effect of Bias Correction of Satellite-Rainfall Estimates on Runoff Simulations at the Source of the Upper Blue Nile. *Remote Sensing*, *6*(7), 6688–6708. https://doi.org/10.3390/rs6076688
Habib, E., Haile, A. T., Tian, Y., & Joyce, R. J. (2012). Evaluation of the High-Resolution CMORPH Satellite Rainfall Product Using Dense Rain Gauge Observations and Radar-Based Estimates. https://doi.org/10.1175/JHM-D-12-017.1
Hargreaves, G. H., Asce, F., & Allen, R. G. (2003). History and Evaluation of Hargreaves Evapotranspiration Equation. https://doi.org/10.1061/(ASCE)0733-9437(2003)129:1(53)
Hirt, C., Filmer, M. S., & Featherstone, W. E. (2010). Comparison and validation of the recent freely available ASTER-GDEM ver1, SRTM ver4.1 and GEODATA DEM-9S ver3 digital elevation models over Australia. *Australian Journal of Earth Sciences*, *57*(3), 337–347. https://doi.org/10.1080/08120091003677553
Jensen, M. E. (2007). Beyond irrigation efficiency. *Irrigation Science*, *25*(3), 233–245. https://doi.org/10.1007/s00271-007-0060-5
Jiménez-Muñoz, J. C., Cristóbal, J., Sobrino, J. A., Sòria, G., Ninyerola, M., & Pons, X. (2009). Revision of the Single-Channel Algorithm for Land Surface Temperature Retrieval From Landsat Thermal-Infrared Data. *IEEE TRANSACTIONS ON GEOSCIENCE AND REMOTE SENSING*, *47*(1). https://doi.org/10.1109/TGRS.2008.2007125
Jiménez-Muñoz, J. C., Sobrino, J. A., Plaza, A., Guanter, L., Moreno, J., & Martínez, P. (2009). Comparison between fractional vegetation cover retrievals from vegetation indices and spectral mixture analysis: Case study of PROBA/CHRIS data over an agricultural area. *Sensors*, *9*(2), 768–793. https://doi.org/10.3390/s90200768
Kljun, N., Calanca, P., Rotach, M. W., & Schmid, H. P. (2015). A simple two-dimensional parameterisation for Flux Footprint Prediction (FFP). *Geoscientific Model Development*, *8*(11), 3695–3713. https://doi.org/10.5194/gmd-8-3695-2015
Kustas, W. P., Norman, J. M., Anderson, M. C., & French, A. N. (2003). Estimating subpixel surface temperatures and energy fluxes from the vegetation index–radiometric temperature relationship. https://doi.org/10.1016/S0034-4257(03)00036-1
Lian, J., & Huang, M. (2016). Comparison of three remote sensing based models to estimate evapotranspiration in an oasis-desert region. *Agricultural Water Management*, *165*, 153–162. https://doi.org/10.1016/j.agwat.2015.12.001
Liang, S. (2000). Narrowband to broadband conversions of land surface albedo I Algorithms.
Liang, S., Shuey, C. J., Russ, A. L., Fang, H., Chen, M., Walthall, C. L., … Hunt, R. (2002). Narrowband to broadband conversions of land surface albedo: II. Validation.
Liou, Y.-A., & Kar, S. (2014). Evapotranspiration Estimation with Remote Sensing and Various Surface Energy Balance Algorithms—A Review. *Energies*, *7*(5), 2821–2849. https://doi.org/10.3390/en7052821
LSA SAF. (2011). Down-welling Surface Shortwave Flux (DSSF): Product User Manual, *7*(2), 1–30.
Ma, W., Hafeez, M., Rabbani, U., Ishikawa, H., & Ma, Y. (2012). Retrieved actual ET using SEBS model from Landsat-5 TM data for irrigation area of Australia. *Atmospheric Environment*, *59*, 408–414. https://doi.org/10.1016/j.atmosenv.2012.05.040
Mekonnen, M. M., Hoekstra, A. Y., & Becht, R. (2012). Mitigating the Water Footprint of Export Cut Flowers from the Lake Naivasha Basin, Kenya. *Water Resources Management*, *26*(13), 3725–3742. https://doi.org/10.1007/s11269-012-0099-9
Mueller Wilm, E. (2016). Sen2Cor Configuration and User Manual. Retrieved from http://step.esa.int/thirdparties/sen2cor/2.3.0/[L2A-SUM] S2-PDGS-MPC-L2A-SUM [2.3.0].pdf

Muthuwatta, L. P., Ahmad, M. ud D., Bos, M. G., & Rientjes, T. H. M. (2010). Assessment of water availability and consumption in the Karkheh river basin, Iran-using remote sensing and geo-statistics. *Water Resources Management*, *24*(3), 459–484. https://doi.org/10.1007/s11269-009-9455-9

Njuki, S. M. (2016). Assessment of Irrigation Performance by Remote Sensing in the Naivasha Basin , Kenya. ITC MSc Thesis. University of Twente.

Odongo, V. O., Mulatu, D. W., Muthoni, F. K., van Oel, P. R., Meins, F. M., van der Tol, C., … van der Veen, A. (2014). Coupling socio-economic factors and eco-hydrological processes using a cascade-modeling approach. *Journal of Hydrology*, *518*, 49–59. https://doi.org/10.1016/j.jhydrol.2014.01.012

Perry, C., Steduto, P., Allen, R. G., & Burt, C. M. (2009). Increasing productivity in irrigated agriculture: Agronomic constraints and hydrological realities. *Agricultural Water Management*, *96*(11), 1517–1524. https://doi.org/10.1016/j.agwat.2009.05.005

Ren, X., Qu, Z., Martins, D. S., Paredes, P., & Pereira, L. S. (2016). Daily Reference Evapotranspiration for Hyper-Arid to Moist Sub-Humid Climates in Inner Mongolia, China: I. Assessing Temperature Methods and Spatial Variability. *Water Resources Management*, *30*(11), 3769–3791. https://doi.org/10.1007/s11269-016-1384-9

Singh, R., Senay, G., Velpuri, N., Bohms, S., Scott, R., & Verdin, J. (2013). Actual Evapotranspiration (Water Use) Assessment of the Colorado River Basin at the Landsat Resolution Using the Operational Simplified Surface Energy Balance Model. *Remote Sensing*, *6*(1), 233–256. https://doi.org/10.3390/rs6010233

Sobrino, J. A., Jiménez-Muñoz, J. C., & Paolini, L. (2004). Land surface temperature retrieval from LANDSAT TM 5. https://doi.org/10.1016/j.rse.2004.02.003

Su, H., McCabe, M. F., Wood, E. F., Su, Z., Prueger, J. H., Su, H., … Prueger, J. H. (2005). Modeling Evapotranspiration during SMACEX: Comparing Two Approaches for Local- and Regional-Scale Prediction. *Journal of Hydrometeorology*, *6*(6), 910–922. https://doi.org/10.1175/JHM466.1

Su, Z. (2002). The Surface Energy Balance System (SEBS) for estimation of turbulent heat fluxes. *Hydrology and Earth System Sciences*, *6*(1), 85–99.

Tol, C. Van Der, Timmermans, W., Corbari, C., Carrara, A., Timmermans, J., & Su, Z. (2015). An Analysis of Turbulent Heat Fluxes and the Energy Balance During the REFLEX Campaign. *Acta Geophysica*, *63*(6), 1516–1539. https://doi.org/10.1515/acgeo-2015-0061

USGS, L. 8. (2016). Landsat Update, *10*(1), 6151.

van der Kwast, J., Timmermans, W., Gieske, A., Su, Z., Olioso, A., Jia, L., … de Jong, S. (2009). Evaluation of the Surface Energy Balance System (SEBS) applied to ASTER imagery with flux-measurements at the SPARC 2004 site (Barrax, Spain). *Hydrology and Earth System Sciences*, *13*(7), 1337–1347. https://doi.org/10.5194/hess-13-1337-2009

van der Velde, R., Su, Z., Ek, M., Rodell, M., & Ma, Y. (2009). Influence of thermodynamic soil and vegetation parameterizations on the simulation of soil temperature states and surface fluxes by the Noah LSm over a Tibetan plateau site. *Hydrology and Earth System Sciences Discussions*, *6*(2006), 455–499. https://doi.org/10.5194/hessd-6-455-2009

van Eekelen, M. W., Bastiaanssen, W. G. M., Jarmain, C., Jackson, B., Ferreira, F., van der Zaag, P., … Luxemburg, W. M. J. (2015). A novel approach to estimate direct and indirect water withdrawals from satellite measurements: A case study from the Incomati basin. *Agriculture, Ecosystems and Environment*, *200*, 126–142. https://doi.org/10.1016/j.agee.2014.10.023

von Engeln, A., Teixeira, J., Engeln, A. von, & Teixeira, J. (2013). A Planetary Boundary Layer Height Climatology Derived from ECMWF Reanalysis Data. *Journal of Climate*, *26*(17), 6575–6590. https://doi.org/10.1175/JCLI-D-12-00385.1

Wan, Z. (1996). A generalized split-window algorithm for retrieving land-surface temperature from space. *IEEE Transactions on Geoscience and Remote Sensing*, *34*(4), 892–905. https://doi.org/10.1109/36.508406

Wiernga, J. (1993). Representative roughness parameters for homogeneous terrain. *Boundary-Layer Meteorology*, *63*(4), 323–363. https://doi.org/10.1007/BF00705357

Wu, X., Zhou, J., Wang, H., Li, Y., & Zhong, B. (2015). Evaluation of irrigation water use efficiency using remote sensing in the middle reach of the Heihe river, in the semi-arid Northwestern China. *Hydrological Processes*, *29*(9), 2243–2257. https://doi.org/10.1002/hyp.10365

Zhan, W., Chen, Y., Zhou, J., Wang, J., Liu, W., Voogt, J., … Li, J. (2013a). Disaggregation of remotely sensed land surface temperature: Literature survey, taxonomy, issues, and caveats. *Remote Sensing of Environment*, *131*(19), 119–139. https://doi.org/10.1016/j.rse.2012.12.014

Zhan, W., Chen, Y., Zhou, J., Wang, J., Liu, W., Voogt, J., … Li, J. (2013b). Disaggregation of remotely

sensed land surface temperature: Literature survey, taxonomy, issues, and caveats. *Remote Sensing of Environment*, *131*, 119–139. https://doi.org/10.1016/j.rse.2012.12.014
Zhang, Z., He, G., Wang, M., Long, T., Wang, G., & Zhang, X. (2016). Validation of the generalized single-channel algorithm using Landsat 8 imagery and SURFRAD ground measurements. *Remote Sensing Letters*, *7*(8), 810–816. https://doi.org/10.1080/2150704X.2016.1190475
Zheng, D., van der Velde, R., Su, Z., Booij, M. J., Hoekstra, A. Y., & Wen, J. (2014). Assessment of Roughness Length Schemes Implemented within the Noah Land Surface Model for High-Altitude Regions. *Journal of Hydrometeorology*, *15*(3), 921–937. https://doi.org/10.1175/JHM-D-13-0102.1

APPENDICES

Appendix A: LST downscaling equations for March 11th and 16th

Date	LST downscaling equation
March 11th 2016	$LST_{R1000}(NDVI_{1km}) = 309.59 - 11.262 * NDVI_{R1000}$
March 16th 2013	$LST_{R1000}(NDVI_{1km}) = 307.94 - 4..929 * NDVI_{R1000}$

Appendix B: GPS points for the location of Bowen ratio stations and rainfall gauging stations showing pivots PB3 and pivot PF3.

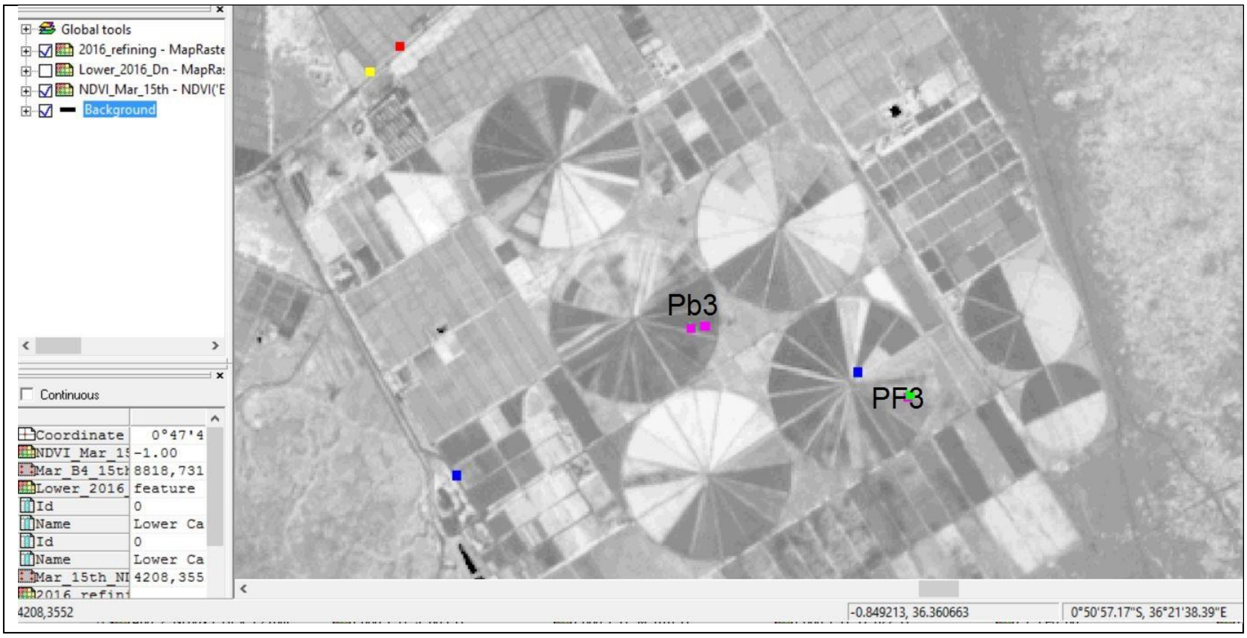

Rainfall gauging station	Coordinates	
Nini Farm	S 00.80042	E 036.40434
KWSTI	S 00.73696	36.4362
Gorge	S 00.84135	E 36.3739
Yacht	210500.0 (X)	9915137.6 (y)
Kijabe	211924.8 (x)	9914724.7 (y)

Appendix C: Crop Coefficient values used for Broccoli (Pivot PB3) and Fine beans (Pivot PF3).

Crop	Kc value range	Crop growth stage at satellite overpass	Kc value used
Broccoli	0.7 to 1.05	Week 5	1.05
Fine Beans	0.4 to 1.05[2]	Week 5	1.05[2]

Appendix D: Monthly water Application Data

Month	Gorge farm	FHK Kingfisher farm
January	194,500	69,900
February	475,710	185,626
March	434,130	163,000
September	470,215	
October	336,025	

Appendix E: Landsat 8 LST derived using the single channel algorithm for 27th September 2016.